

Molecular dynamics simulations of shock compression of nickel: From monocrystals to nanocrystals

H.N. Jarmakani^a, E.M. Bringa^b, P. Erhart^b, B.A. Remington^b,
Y.M. Wang^b, N.Q. Vo^c, M.A. Meyers^{a,*}

^a *Materials Science and Engineering Program, Departments of Mechanical and Aerospace Engineering and Nanoengineering, University of California, 9500 Gilman Drive, San Diego, La Jolla, CA 92093-0418, USA*

^b *Lawrence Livermore National Laboratory, Livermore, CA 94550, USA*

^c *Department of Materials Science and Engineering, University of Illinois, Urbana-Champaign, Urbana, IL 61801, USA*

Received 7 April 2008; accepted 24 July 2008

Available online 6 September 2008

Abstract

Shock compression of mono- and nanocrystalline (nc) nickel is simulated over a range of pressures (10–80 GPa) and compared with experimental results. Contributions to the strain from the various mechanisms of plastic deformation such as partial dislocations, perfect dislocations and twins are quantified in the nc samples. The effect of stress unloading, a phenomenon often neglected in MD simulations, on dislocation behavior is computed. It is shown that a large fraction of the dislocations generated during compression is annihilated upon unloading. The present analysis resolves a disagreement consistently observed between MD computations and experimental results. Analytical models are applied to predict the critical pressures for the cell-to-stacking-fault transition and the onset of twinning as a function of grain-size and stacking-fault energy (through the addition of tungsten). These predictions are successfully compared with experimental results.

© 2008 Acta Materialia Inc. Published by Elsevier Ltd. All rights reserved.

Keywords: Shock compression; Molecular dynamics; Nickel; Nanocrystalline metals; Twinning

1. Introduction

Molecular dynamics (MD) simulations of nanocrystalline (nc) metals are ideally suited for comparison with laser-shock compression experiments because of the similar time and length scales; thus, the combination of experiments and simulations provides valuable insight on the deformation processes involved. It should be pointed out that the difference between mono- and polycrystals in MD resides in the absence and presence of grain boundaries, respectively. The box sizes of the largest simulations being run today are approaching ~300 nm, which is at the upper end of the nc range.

1.1. Single crystals

MD simulations of shock phenomena in perfect face-centered cubic (fcc) single-crystals have been carried out for just over 25 years [1–3]. Most of the simulations to date have used the Lennard–Jones (L–J) 6–12 spline pair-potential [4–7] and the more realistic embedded atom method (EAM) many-body potentials for Cu [8–12]. Holian and Lomdahl [4] and Germann et al. [5,7] showed, using L–J potentials that, at shock strengths above the Hugoniot elastic limit (HEL), shock waves traveling along the [001] orientation resulted in the emission of intersecting Shockley partial dislocations that slipped along all the {111} close-packed planes. Stacking-faults were formed since the trailing partial was never released. The large mobility of the partials at the shock front was such that the plastic wave was always overdriven (i.e. no elastic precursor observed).

* Corresponding author. Tel.: +1 619 534 5698.

E-mail addresses: mameyers@mae.ucsd.edu, mameyers@ucsd.edu (M.A. Meyers).

This dislocation behavior is very similar to the model proposed by Smith [13], except that partial dislocation loops are emitted in MD simulations rather than perfect dislocations as outlined by the Smith model.

Germann et al. [5,7] further studied shock propagation in the other [110] and [111] low index directions, where they observed rather different behavior. An elastic precursor separated the shock front from the plastic region in the [111] case, and solitary wave trains were generated followed by an elastic precursor and a complex plastic zone in the [011] case. In both orientations, trailing partials were emitted leading to full dislocation loops bounded by thin stacking-fault ribbons. These loops were periodically nucleated at the shock front, as proposed by Meyers [14], since they grew at a slower rate than the plastic shock velocity.

Bringa et al. [11] also studied the effect of crystal orientation on the shock Hugoniot along the low index directions ([001], [011] and [111]) using two EAM potentials for Cu [15,16]. The plasticity in the three orientations was qualitatively similar to that of Germann et al. [5,7]. Cao et al. [12] investigated the nonsymmetric [221] orientation, where a two-wave (elastic and plastic) structure was observed. The deformation features and shock Hugoniot obtained compared very well with experimental results. However, upon comparing the density of the deformation features with experimental observations in recovered samples, they found that dislocation densities in simulations were several orders of magnitude higher. Two reasons were suggested by Cao et al. [12] for the difference: (i) the much shorter rise time in molecular dynamics simulations, and (ii) the post-shock relaxation and recovery processes that take place in real experiments.

To the knowledge of the authors, only one paper, by Kum [17], analyzes the deformation features in shock-compressed single-crystalline Ni along the three low-indexed orientations. Two Morse-type pair potentials and one EAM potential were used in that work. However, the study is limited to one piston velocity and does not calculate the Hugoniot obtained from MD.

1.2. Nanocrystals

In contrast with monocrystals, numerous investigators have carried out molecular dynamics studies of plastic deformation in nc metals (e.g. [18–23]). In two classic papers, Van Swygenhoven et al. [18,20] studied the response of nc Ni (grain size 3–12 nm) under uniaxial loading; they observed intergranular sliding at the smaller grain sizes and dislocation emission from grain boundaries at the larger grain sizes. They used the Finnis–Sinclair Ni potential [24]. Schiøtz et al. [19,22] studied the behavior of nc Cu (grain size 3–7 nm) under uniaxial deformation and observed softening as the grain size decreased beyond a threshold due to grain-boundary sliding. The effective medium theory was used to describe the forces between the atoms [25,26]. Yamakov et al. [21] studied nc Al (grain size 20–70 nm) under tensile loading using a many-body inter-

atomic potential [27] and observed that, contrary to its coarse-grained counterpart, mechanical twinning was a key deformation mechanism.

Studies on the response of nc metals under shock compression are limited to mostly Cu [28–30] and Al [21]. MD studies on the shock response of Ni have not been carried out to date. Bringa et al. [28] studied shock compression of nc Cu. An increase in strength during shock loading was observed due to the suppression of grain-boundary sliding under compression, which was identified as being due to a Mohr–Coulomb-like mechanism. As pressure increased, a shift in the maximum hardness to lower grain sizes was observed. However, beyond a critical pressure, increased dislocation activity due to higher temperatures resulted in a drop in strength. Their simulations revealed both perfect and partial dislocations as well as nano-twins.

In this study, we analyze the response of mono- and nanocrystalline Ni governed by an EAM potential. The shock Hugoniot in the [001] direction is first determined and compared to experimental results (Section 3). Upon verifying the conformity of the potential with experimental results, we then study the effect of shock compression as well as release on nc Ni (grain-size 5 and 10 nm). MD results are compared to laser-shock experiments carried out on nc Ni at LLNL [31,32] as part of the National Ignition Facility (NIF) program (Section 5). Analytical constitutive models are utilized to predict the critical pressures at which a stacking-fault transition occurs in single-crystalline Ni (Section 4) and a twinning transition occurs in nc Ni and compared with MD simulations and experimental observations (Section 6).

2. Computational methods

The MD simulations were carried out using the Large-scale Atomic/Molecular Massively Parallel Simulator (LAMMPS) code [33] and a Ni EAM potential developed by Mishin et al. [34]. This potential was fitted to provide a stacking-fault energy (SFE) of 125 mJ m⁻² [35]. The EAM views each atom as embedded in a host lattice consisting of all other atoms. Each atom in the system is viewed as an impurity that is part of a host of all other atoms. The “embedding energy” of the impurity is determined by the electron density of the host before the impurity is added. The energy of an atom (or impurity), i , is represented as a function of the electron density at the atom site plus an electrostatic interaction due to the host [36,37]:

$$E_i = F_i[\rho_i(R_i)] + \frac{1}{2} \sum_j \varphi(R_{ij}), \quad (1)$$

where ρ_i is the electron density of the host without atom i , φ is the short-range electrostatic pair potential as a function of the distance R_{ij} between atoms i and j , and F is the “embedding energy”, which is a function of the host

electron density, ρ_i , induced at site i by all other atoms in the system. The total energy is the sum over all individual contributions

$$E_{\text{tot}} = \sum_i E_i = \sum_i F_i[\rho_i(R_i)] + \frac{1}{2} \sum_{ij} \varphi(R_{ij}). \quad (2)$$

Fig. 1a shows the total energy per atom as a function of the lattice parameter determined by this potential (both in uniaxial and hydrostatic compression), with the minimum at the lattice spacing of Ni, $a_o = 0.352$ nm. Fig. 1b shows the pressure-specific volume relationship of the potential as well as the experimental Hugoniot obtained from Rice et al. [38]. The potential (in hydrostatic compression) compares fairly well with the experimental data up to pressures of ~ 130 GPa, where it begins to significantly deviate. As a result, we have limited our study to shock pressures below

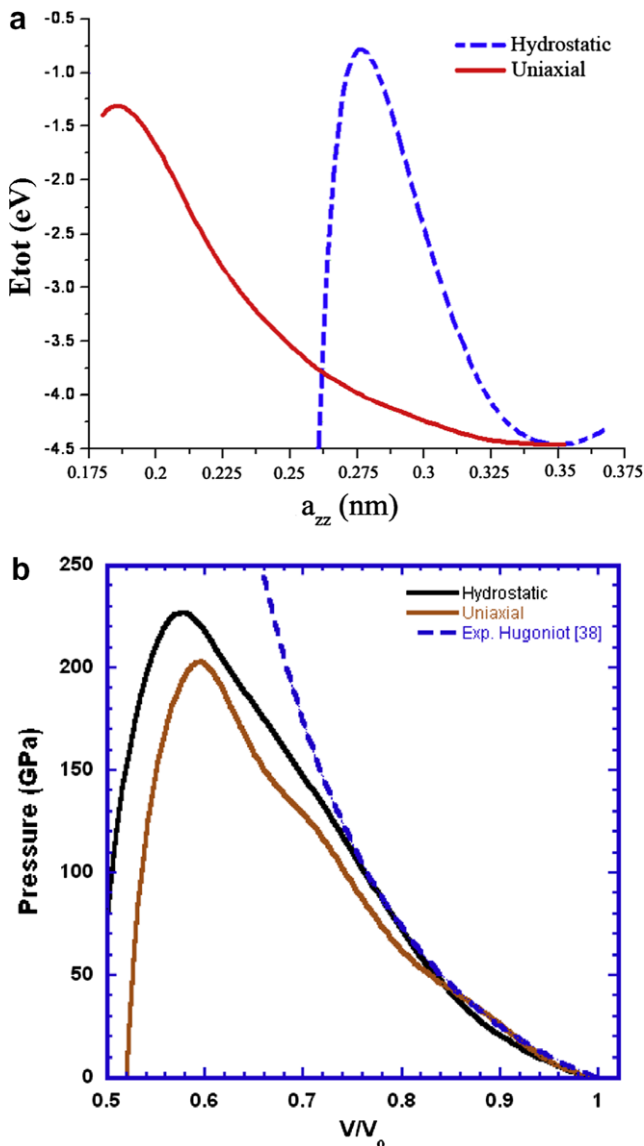


Fig. 1. (a) Total energy per atom vs. the lattice parameter defined by the Mishin–Farkas potential; (b) P – V relation of Mishin–Farkas compared with experimental Hugoniot.

this value. It should be noted that the drop in the P – V relation at $V/V_o \sim 0.58$ is simply due to the fact that the potential is not defined beyond these values.

The [001] monocrystalline Ni sample consisted of 2×10^6 atoms and had dimensions of $17.6 \text{ nm} \times 17.6 \text{ nm} \times 70.4 \text{ nm}$ ($50 \times 50 \times 200$ unit cells) – large enough to calculate the shock Hugoniot and study the early stages of shock-induced plasticity. The three coordinate axes were oriented in the [100], [010] and [001] directions. In order to minimize edge effects, periodic boundary conditions were imposed on the lateral surfaces, and the surfaces normal to the shock-wave propagation direction were set as free surfaces. The shock waves were produced by driving a piston, defined by a few atomic planes, into the sample at a specific velocity U_p , similar to other studies [11,12]. Two nc samples were used in this study, one having a grain size of 5 nm and the other 10 nm. The 5 nm grain-sized sample consisted of 1,980,372 atoms ($50 \times 50 \times 200$ unit cells, $17.6 \text{ nm} \times 17.6 \text{ nm} \times 70.4 \text{ nm}$), and the 10 nm grain-sized sample had 7,942,605 atoms ($100 \times 100 \times 200$ unit cells, $35.2 \text{ nm} \times 35.2 \text{ nm} \times 70.4 \text{ nm}$). Prior to compression, the specimens were first equilibrated to achieve a minimum energy state, and the initial temperature was set as 5 K. The velocity of the shock wave, U_s , was measured by analyzing the shock front propagation in the sample at different time steps, and the shock pressure was calculated from the following Hugoniot relation [39]:

$$P_{\text{shock}} = \rho_o U_s U_p. \quad (3)$$

3. Shock propagation and defect generation in [001] monocrystalline Ni

The HEL occurs at a shock pressure of ~ 40 GPa, at which stacking-faults begin to develop as the key deformation feature. Interestingly, experimental studies have observed twinning to occur in single-crystalline Ni at a comparable shock pressure of ~ 35 GPa [40–42]. Above the HEL, the shock wave splits into an elastic precursor and a plastic front. This behavior is very different from previous MD studies on [001] fcc single-crystals, where the plastic front is usually overdriven [5–7,11,12]. Fig. 2a shows the single front shock wave propagating through the sample at 6, 8 and 10 ps, with a particle velocity, U_p , equal to 0.6 km s^{-1} , below the HEL; Fig. 2b shows the two-front wave for $U_p \sim 0.9 \text{ km s}^{-1}$, above the HEL.

Fig. 3a compares the P – U_p relationship determined from the current MD simulations with experimental results [14]. Clearly, the P – U_p relationships in both cases are very similar allowing meaningful comparisons between the two. Fig. 3b presents both the MD and experimental U_s – U_p relations. At a piston/particle velocity of $\sim 0.7 \text{ km s}^{-1}$ (just above the HEL), the U_s for MD splits into a faster elastic wave and a lagging plastic wave, the average of the two being closer to the experimental U_s data. As the piston velocity increases in MD, the velocity of the plastic wave increases, whereas that of the elastic wave decreases; at a

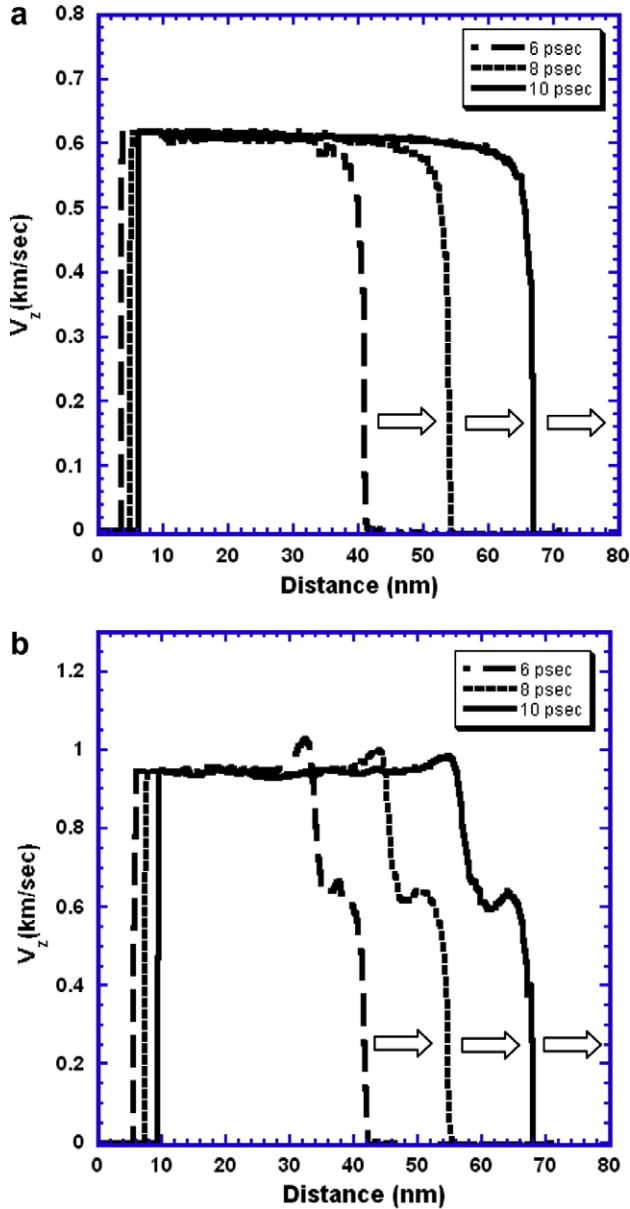


Fig. 2. (a) Piston/particle velocity at 6, 8 and, 10 ps vs. distance (below the HEL) for $P \sim 35$ GPa; (b) piston/particle velocity at 6, 8 and 10 ps vs. distance (above the HEL) for $P \sim 48$ GPa.

piston/particle velocity of $\sim 1.5 \text{ km s}^{-1}$, the shock wave becomes overdriven.

It was initially rationalized that this two-wave structure may be the result of the high SFE of Ni, causing the second trailing partial to be emitted and slowing down the plastic wave, thereby allowing the elastic wave to lead. But, upon further investigation of the samples, this was found not to be the case. As with previous studies on [001] fcc single-crystals, only partial dislocation loops are emitted. Fig. 4a is a cross-sectional view through a sample shocked with $U_p = 0.786 \text{ km s}^{-1}$ (just above the HEL) showing stacking-fault formation behind the shock front. Note the $\langle 110 \rangle$ family of directions along which the stacking-faults are oriented. Fig. 4b shows, from a different angle, the for-

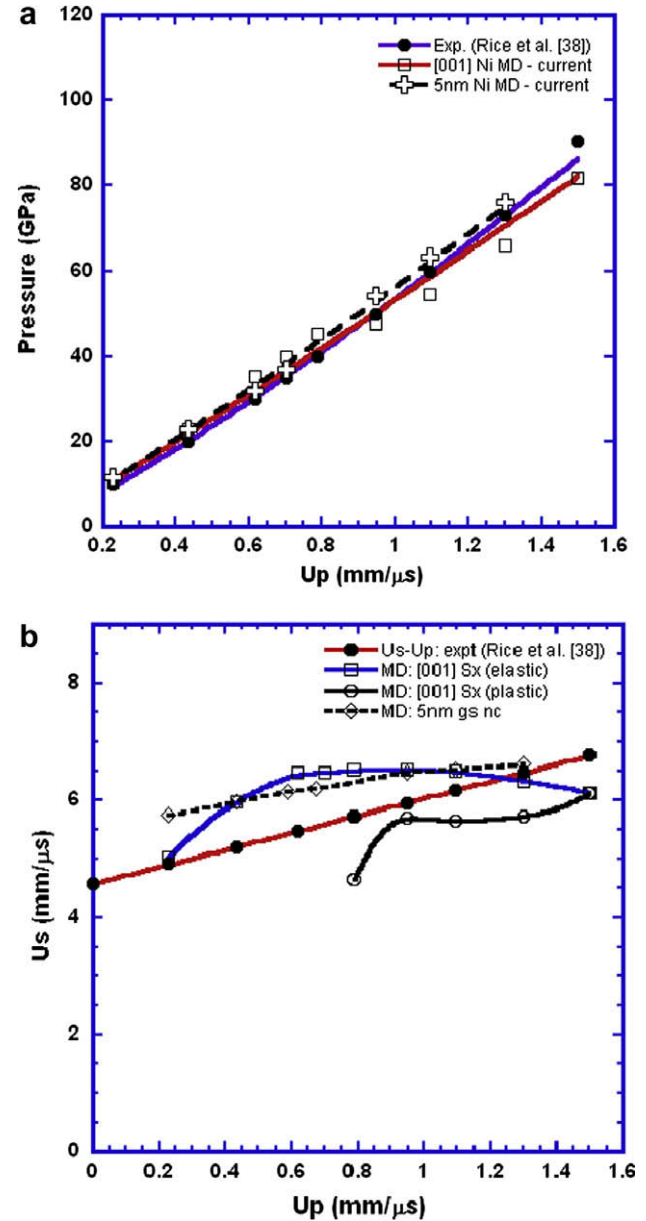


Fig. 3. (a) $P-U_p$ relationship for Ni, both MD and experimental data by Rice et al. [38]; (b) U_s-U_p relationship, both MD and experimental data.

mation of the lagging plastic zone (also for the case $U_p = 0.786 \text{ km s}^{-1}$), whereby the elastic precursor outruns the partial dislocations and new partial dislocation loops are generated just behind the leading elastic wave front. This picture is analogous to the homogeneous dislocation model [14], reproduced in Fig. 4c. It should be noted that, for better visualization, the “centrosymmetry” parameter is used, to identify defective atoms (dislocation cores and stacking-faults). It is of the form [43],

$$C = \sum_{i=1}^6 |\vec{r}_i + \vec{r}_{i+6}|^2, \quad (4)$$

where \vec{r}_i and \vec{r}_{i+6} are the vectors from the central atom to the opposite pair of nearest neighbors (six pairs in an fcc

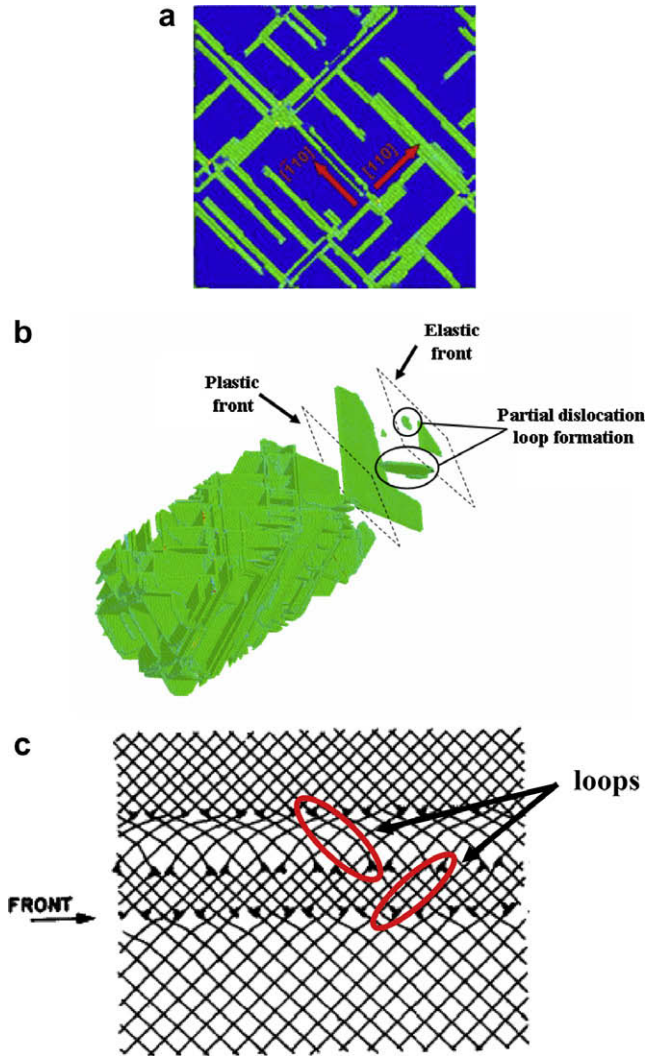


Fig. 4. Shock compression of Ni along [001]; $U_p = 0.786$ km/s; (a) stacking-faults, view along longitudinal z direction; (b) plastic and elastic zone formation; notice formation of dislocation loops; (c) dislocation interface in homogeneous generation model [14].

system, i.e. the coordination number). Atoms in perfect fcc lattice positions have C equal to zero, whereas atoms having faulty stacking will generate a nonzero C .

The shear stresses in the sample were studied as the shock pressure was increased. The shear stress was determined by the following equation since off-diagonal terms are negligible:

$$\tau_{\text{shear}} = \frac{1}{2} \left[\sigma_{zz} - \frac{1}{2} (\sigma_{xx} + \sigma_{yy}) \right], \quad (5)$$

where σ_{zz} is the normal stress in the shock propagation direction and σ_{xx} and σ_{yy} are transverse normal stresses. Fig. 5a shows the z -component of stress (σ_{zz}) and the shear stress plotted against sample depth at 10 ps into the simulation ($U_p \sim 0.945$ km s⁻¹). Fig. 5b shows that the shear stress in the sample increases up to $\sigma_{zz} \sim 70$ GPa, after which it drops. The maximum value of the shear stress, $\tau_s \sim 7$ GPa, is consistent

with the stress required to nucleate shear loops, equal to $\sim G/10$ (for Ni, $G = 76$ GPa). This drop coincides with the HEL (total pressure ~ 40 GPa), where plasticity sets in.

The defect spacing as a function of shock pressure was analyzed in order to quantify the induced plasticity (Fig. 6a). Clearly, the stacking-fault spacing decreases as the shock pressure increases. Data for Cu from Cao et al. [12] are plotted as well. Holian and Lomdahl [4] introduced two fundamental deformation parameters: shock-induced plasticity and shock strength. Shock-induced plasticity is defined as a_0/l , where a_0 is the lattice parameter ($= 0.352$ nm for Ni), and l is the average lattice spacing between stacking-faults. They defined shock strength as the ratio between particle velocity and speed of sound in the material, U_p/C_0 ($C_0 = 4.581$ km s⁻¹ for Ni). This shock-induced plasticity as a function of shock strength is plotted in Fig. 6b. MD data on Cu from Cao et al. [12], predictions from the homogeneous nucleation model of Meyers [14], and experimentally measured data from Murr [44] are also shown on the plot. For the results from Meyers [14] and Murr [44], the dislocation spacing, l , was extracted from the reported dislocation densities ρ , using the equation $l = \sqrt{\rho^{-1}}$. The plasticity data from the current MD results are consistent with those of Cao et al. [12], Holian and Lomdahl [4], and analytical calculations by Meyers [14]. The experimentally determined shock plasticity of Ni from Murr [44] is, however, lower than the theoretical and MD results by an order of magnitude. This suggests that relaxation processes are clearly at play in real experiments, resulting in lower dislocation densities, as will be shown below.

The effect of release (stress unloading) in the MD simulations was studied for comparison with experiments. The piston was released after 10 ps and the pressure ($P_{\text{tot}} = f(\sigma_{xx}, \sigma_{yy}, \sigma_{zz})$) was allowed to retract back to zero. Interestingly, almost all the partial dislocation loops disappear. The spacing between the few remaining stacking-faults was measured, and the resulting residual plasticity was calculated. Fig. 6b shows the MD plasticity after release; an order of magnitude drop is evident, synonymous with the experimental data by Murr [44]. The pressure rise due to compression and the accompanying drop due to release are shown in Fig. 7 for the case of $U_p = 1.1$ km s⁻¹. Only the defective atoms are shown.

4. Dislocation loop analysis: stacking-fault transition

The nucleation of dislocation loops was first treated by Cottrell [45] and later further developed by Xu and Argon [46], Rice [47] and others. A mechanism was also proposed by Khantha and Vitek [48] for the generation of dislocations under extreme conditions. At pressures above 3–3.2 GPa, the activation energy for loop nucleation is lower than the thermal energy; thus, nucleation becomes thermally activated, whereas it is not activated under conventional deformation at ambient temperature.

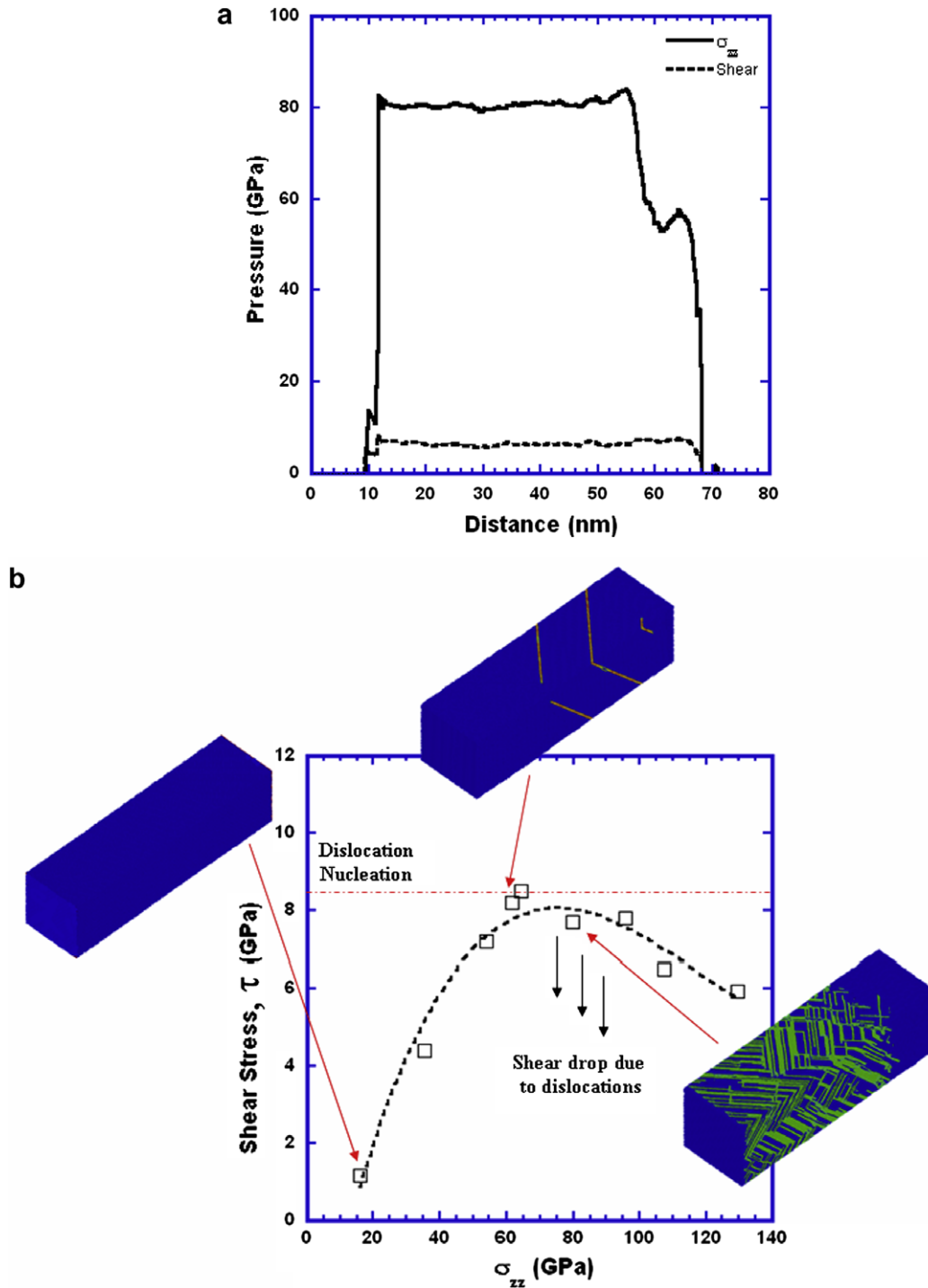


Fig. 5. (a) Shear stress and σ_{zz} vs. sample depth, $U_p \sim 0.945$ km/s; (b) shear stress vs. σ_{zz} .

As previously mentioned, Meyers [14] proposed in 1978 that dislocations in shock compression were homogeneously generated by loop expansion. Fig. 8a shows shear loops generated on {111} planes making an angle of 54.7° with the shock compression plane, (001). Whereas the nucleation and growth of perfect dislocation loops can lead to the formation of a cellular structure after multiple cross-slip and relaxation of the dislocation configurations, the stacking-fault packets observed in

shock compression above 20 GPa cannot be accounted for by this mechanism. The corresponding nucleation of partial loops is shown in Fig. 8b.

The calculation recently introduced by Meyers et al. [49] for the energetics of nucleation of partial dislocation loops in Cu is extended here for Ni. The analytical development is reproduced for the sake of clarity and continuity. The critical radius, r_c (Fig. 8), can be found from the maximum of the energy vs. radius curve [45,50],

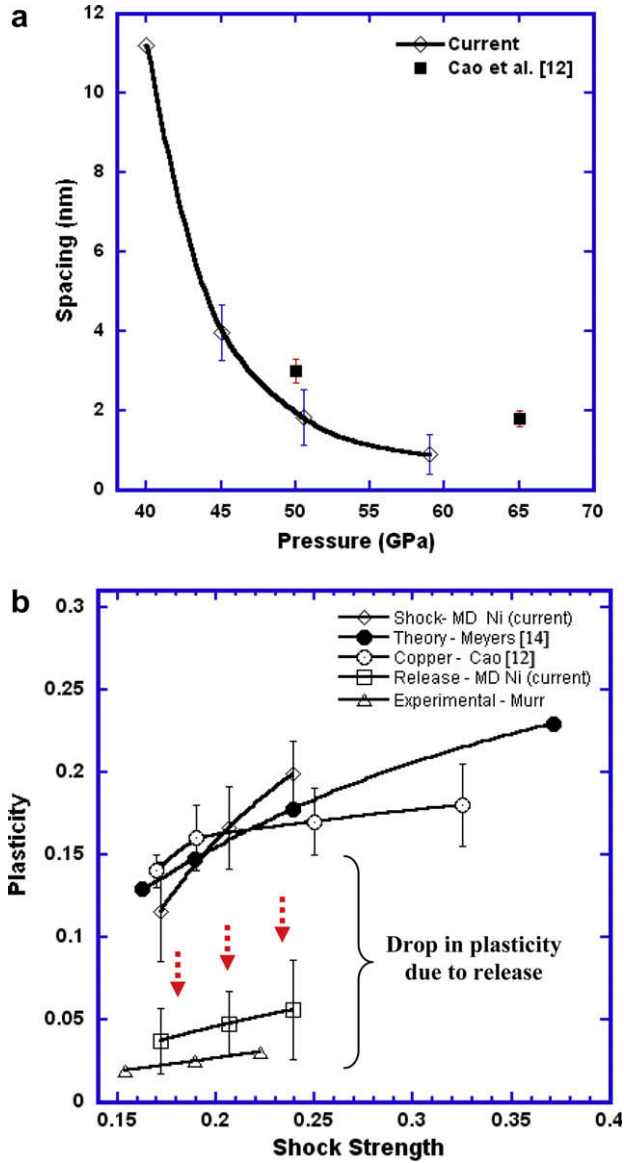


Fig. 6. (a) Spacing of dislocations vs. shock pressure; (b) Holian-Lomdahl [4] plot showing plasticity (a_o/l) vs. shock strength (U_p/C_o).

$$\frac{dE}{dr} = 0. \quad (6)$$

The total energy of a perfect dislocation loop with radius r is the sum of the increase of the energy E_1 , due to a circular dislocation loop (assumed to be one-half edge and one-half screw), and the work W carried out by the applied stress τ on the loop (assumed to be circular):

$$E = E_1 - W = \frac{1}{2} G b^2 r \left(\frac{2-v}{1-v} \right) \ln \left(\frac{2r}{r_o} \right) - \pi r^2 \tau b, \quad (7)$$

where v is Poisson's ration, G the shear modulus, b the Burgers vector and τ the shear stress. The critical radius is obtained by taking the derivative of Eq. (7) with respect to r and applying Eq. (6):

$$r_c = \frac{G b}{8 \pi \tau} \left(\frac{2-v}{1-v} \right) \left(\ln \frac{2r_c}{r_o} + 1 \right). \quad (8)$$

To obtain the total energy of the partial dislocation loop (Fig. 8b), both the energy of the stacking-fault, E_2 , and work done by shear stress, W , have to be incorporated:

$$E = E_1 + E_2 - W. \quad (9)$$

Substituting the values of E_1 , E_2 and W into Eq. (9):

$$E = \frac{1}{4} G b_p^2 r \left(\frac{2-v}{1-v} \right) \ln \left(\frac{2r}{r_o} \right) + \pi r^2 \gamma_{sf} - \pi r^2 \tau b_p, \quad (10)$$

where γ_{sf} is the SFE and b_p is the Burgers vector for a partial dislocation. The critical radius is obtained by the same method:

$$r_c = \frac{G \left(\frac{b}{\sqrt{3}} \right)^2}{8 \pi \left(\frac{\tau b}{\sqrt{3}} - \gamma_{sf} \right)} \left(\frac{2-v}{1-v} \right) \left(\ln \frac{2r_c}{r_o} + 1 \right). \quad (11)$$

For Ni, we have $v = 0.31$, $\gamma_{sf} = 130 \text{ mJ m}^{-2}$ and $G = 76 \text{ GPa}$ at zero pressure. G changes with pressure as follows [51]:

$$G = 76 + 1.37P(\text{GPa}). \quad (12)$$

The Burgers vector, b_o , at $P = 0$ is equal to 0.249 nm; it changes with shock pressure as:

$$b = \left[\frac{C_o^2}{2PS^2V_o} \left(\sqrt{1 + \frac{4PSV_o}{C_o^2} + \frac{2S(S-1)V_oP}{C_o^2}} - 1 \right) \right]^{1/3} b_o, \quad (13)$$

where C_o is 4.581 km s^{-1} , S is 1.44 and V_o is the specific volume of Ni ($\text{m}^3 \text{ kg}^{-1}$) at zero pressure. The shear stress, τ , assuming elastic loading, can be calculated from the shock pressure through Eq.(6):

$$\tau = -\frac{1-2v}{2(1-v)}P. \quad (14)$$

The calculated results are shown in the normalized plot of Fig. 9a (pressure and critical radius are divided by the shear modulus and Burgers vector, respectively). It can be seen that the critical radius for perfect dislocations is lower than for partial dislocations at lower pressures; with increasing pressure, partial dislocations become more favorable. The predicted transition pressure for Ni is $\sim 27 \text{ GPa}$, close to the experimentally observed twinning transition pressure, 35 GPa [40–42,44], and about half the pressure at which stacking-faults began to appear in our Ni MD study. The predicted transition pressure for Cu, $\sim 5 \text{ GPa}$, is also significantly lower than both MD and experimentally observed results [52,53]. Experimental evidence for the cell-stacking-fault transition has been gradually amassing for Cu, and the transmission electron micrograph of Fig. 9b is clear. For Ni, the transition pressure is much higher (27 GPa). This exceeds the critical pressure for twinning ($P = 16 \text{ GPa}$, calculated in Section 6) and is consistent with the absence of stacking-fault observations in shock-compressed Ni. Thus, one has the following defect regimes as P is increased:

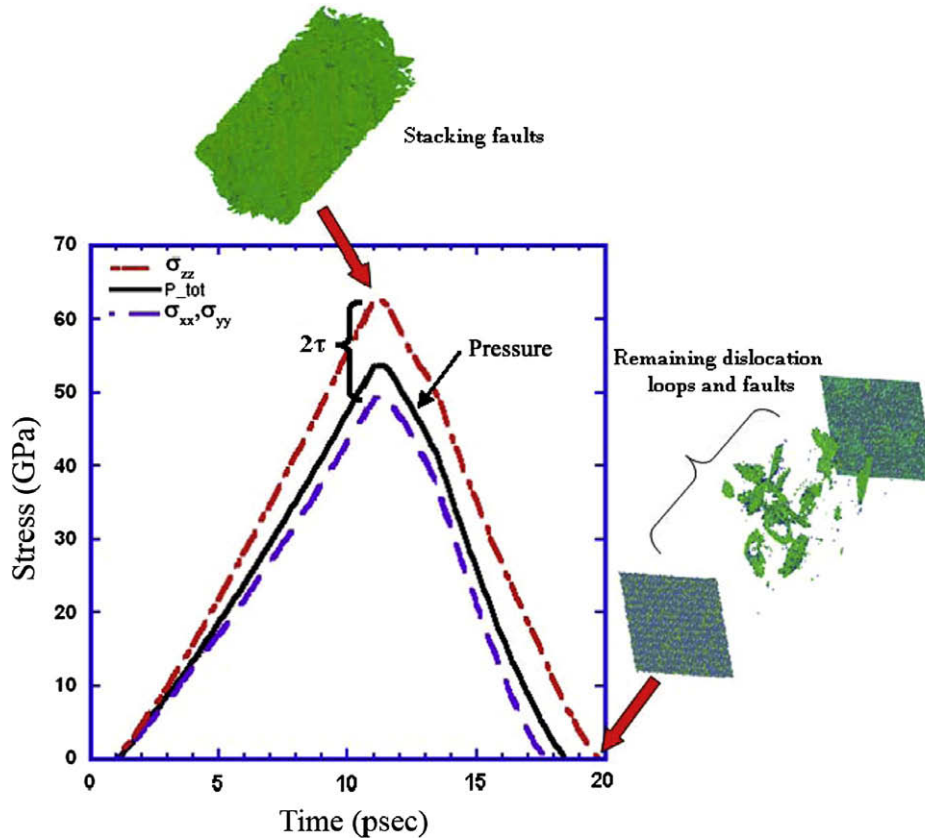


Fig. 7. P_{tot} , σ_{xx} , σ_{yy} , σ_{zz} vs. time step, $U_p = 1.094$ km/s.

Cu: cells → stacking-faults → twins
 Ni: cells → twins

It should be noted that these results are not in complete agreement with our MD computations and previous work [3–7,55], which predict perfect dislocations for shock along [111] and partials and stacking-faults along [001]. Our release simulations do show, however, that very few perfect dislocation loops survive after the stacking-faults are allowed to relax (Fig. 7) as the pressure drops to zero.

The transmission electron micrograph from Fig. 9b comes from a quasi-isentropic laser compression experiment at a nominal pressure of 24 GPa for a [001] Cu monocrystal [54]. One sees adjacent regions of stacking-faults and dislocation cells, with a well-defined discrete boundary. This was a fortuitous observation and the transition can be caused by pressure or strain rate. Nevertheless, it clearly illustrates the dual nature of the microstructure induced.

5. MD simulations of shock in nc Ni

The 5 nm grain-sized sample was subjected to piston velocities between 0.2 and 1.3 km s⁻¹, and its Hugoniot was found to be very close to that of the monocrystalline sample. Fig. 3a shows the consistency of the $P-U_p$ relationship for the 5 nm grain-sized samples with both experimen-

tal and single-crystal MD results. The shock velocity, U_s is slightly higher in the nc sample, as seen in Fig. 3b. Fig. 10a provides an illustration of the shock wave for $U_p = 0.67$ km s⁻¹ as it traverses the sample (average velocity vs. distance). The corresponding shock pressure within the sample is ~38 GPa, which is right at the HEL limit for the monocrystalline sample. Since grain boundaries (i.e. defects) exist in the sample, the HEL is lower than that in the single crystal. A single-wave structure is evident and not a two-wave structure as seen in the single-crystalline results. This may be due to the fact that the particle velocities vary from grain to grain, introducing fluctuations in the front that do not allow the plastic and elastic components to be resolved. In comparison with the single-crystal profiles shown in Fig. 2a, the front thickness is increased from ~2 to ~10 nm. Fig. 10b shows the nc sample at 0 ps, after it has been relaxed to minimize its internal energy prior to shock propagation (left) and after the shock-wave has traveled for 10 ps (right). Grain boundaries act as sources and sinks for partial dislocations, leaving stacking-faults behind as they travel through the grains. Two of these are marked for clarity. This defect configuration is similar to the one observed by Van Swygenhoven et al. [18,20] and Bringa et al. [28]. Leading partials are mainly emitted from the grain boundaries, and trailing partials are seldom released. Limited evidence of twinning was also observed. Fig. 10c is a three-dimensional view of the sample.

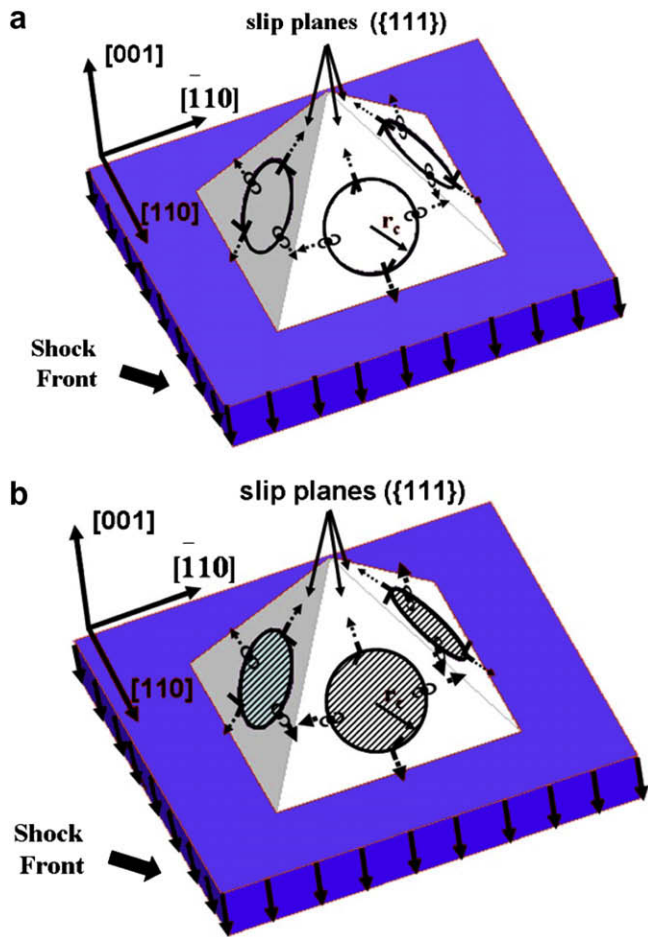


Fig. 8. Nucleation of dislocation loops at slip planes behind the shock front, which is in red (propagation along [001]): (a) perfect dislocations and (b) partial dislocations (adapted from [49]).

5.1. Deformation analysis: comparison of MD with experiments

A quantitative analysis of the deformation mechanisms was carried out on three samples that were shocked using the same piston/particle velocity of 0.67 km s^{-1} ($\sim 38 \text{ GPa}$): 5 nm Ni, 10 nm Ni and 10 nm Cu (Cu Mishin potential [16]). The three samples provide the means to study the effect of grain size and a different potential on the deformation behavior. Contributions to the effective strain introduced by shock compression from the various mechanisms of plastic deformation were calculated by determining the relative motion between nearest neighbor pairs of atoms, and resolving this motion along the strain axis. The procedure to quantify the dislocation contributions to the total plastic strain consists of three steps. The first step locates nearest neighbor atom pairs that have been sheared on glide planes and assigns local Burgers vectors responsible for the shearing. This step requires correction for the strain caused by atom pairs that are cut by multiple dislocations with different Burgers vectors. The second step distinguishes atoms in grain interiors that are cut by lattice dislocations from those that are involved in

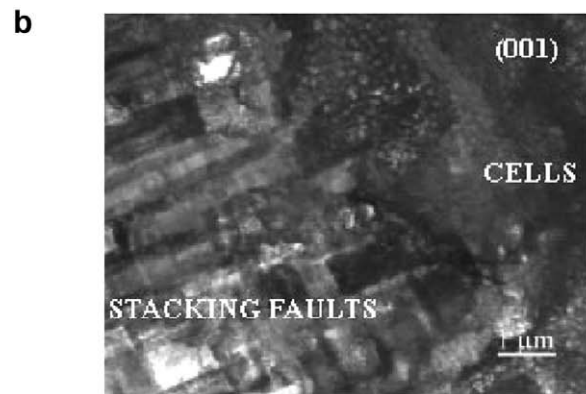
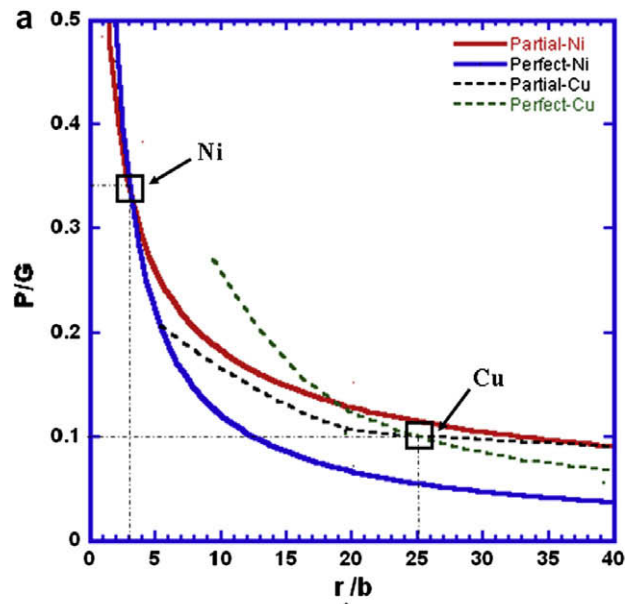


Fig. 9. (a) Critical radius of perfect and partial dislocations for Ni and Cu decreases with shock pressure; (b) stacking-faults and cells in the same TEM micrograph of laser-shocked copper demonstrating that there is a critical value for transition.

grain-boundary mechanisms. The third step evaluates the strain caused by the motion of the dislocations identified. Detailed procedures can be found in Refs. [56,57]. Using this method, the contributions from partial dislocations, perfect dislocations, multiple dislocations on the same slip plane, and twinning can be identified. The difference between the total plastic deformation and these other contributions can then be attributed to grain-boundary sliding.

Fig. 11 shows the three shocked samples. The color code is as follows: the blue atoms are not displaced and are in their original minimum energy state; the green atoms are displaced by the Burgers vector of a Shockley partial; the red atoms are displaced by a Burgers vector of a perfect dislocation; and the orange atoms are displaced by a Burgers vector larger than that of a perfect dislocation. Table 1 lists the strains due to perfect and partial dislocations in three nc samples: 5 nm Ni, 10 nm Ni and 10 nm Cu. Column (1) gives the strain contribution of twinning; columns (2) and (3) provide the contribution due to one partial and

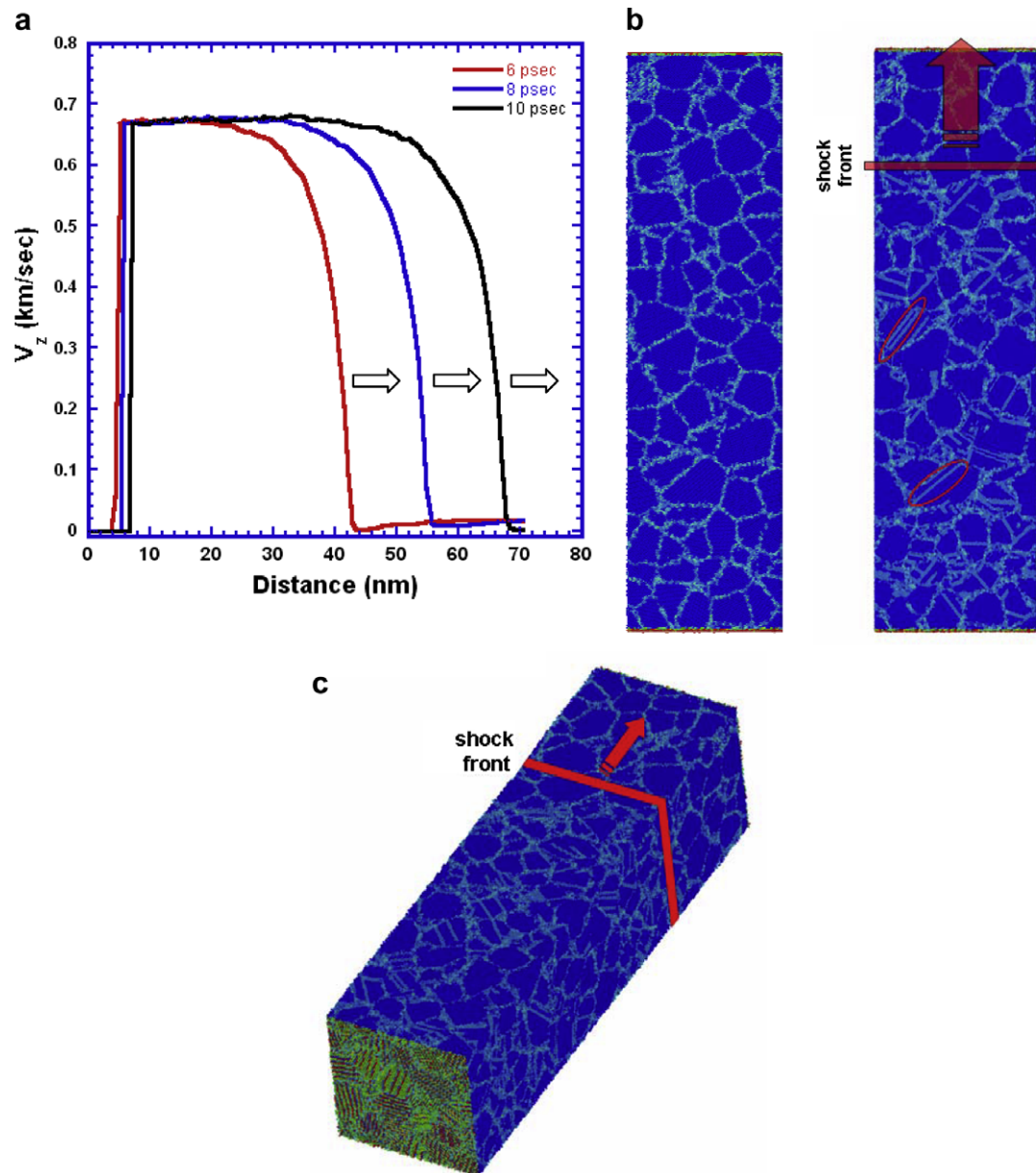


Fig. 10. Shock compression of nanocrystalline specimen, g. s. = 5 nm, $U_p = 0.67$ km/s; (a) z-component of velocity vs. distance; (b) 5 nm grain-sized sample at 0 ps and 10 ps; (c) three-dimensional view of sample at 10 ps.

one perfect dislocation in a slip plane, respectively. Column (4) provides the contribution of more than one dislocation per slip plane. Column (5) is the total strain due to dislocations (= (2) + (3) + (4) + (5)). The last column (6) gives the strain due to grain-boundary shear. For the 5 nm Ni, the total shock strain in the sample was calculated to be ~ 0.13 . Fig. 12 shows the shock strain as a function of U_p in the monocrystalline and nc samples as well as the applied strain rates. The total strain contribution due to dislocations (0.014) is dominated by partials, which makes up $\sim 60\%$ of the total strain due to dislocations; perfect dislocations account for $\sim 10\%$. The contribution due to twinning is 26%. By subtracting the strain due to dislocations from the total strain, one obtains the strain due to grain-

boundary sliding, 0.116; this represents approximately $\sim 90\%$ of the total.

In the case of the 10 nm samples, the strain contribution due to partials is 63% for Ni and 56% for Cu. Perfect dislocations account for 17.2% of the dislocation strain in Ni and 21% in Cu. The twinning contribution is greater in Cu, 19% as compared to 16% in Ni. The greater incidence of twins is to be expected since the SFE of Cu is significantly lower. Grain-boundary sliding accounts for approximately 58% of the total shock strain in both 10 nm Ni and Cu in comparison with 90% for 5 nm Ni, signifying that it becomes more difficult for larger grains to slide past one another under compression. Note that the front portions of the 10 nm Cu and Ni samples do not show the grain

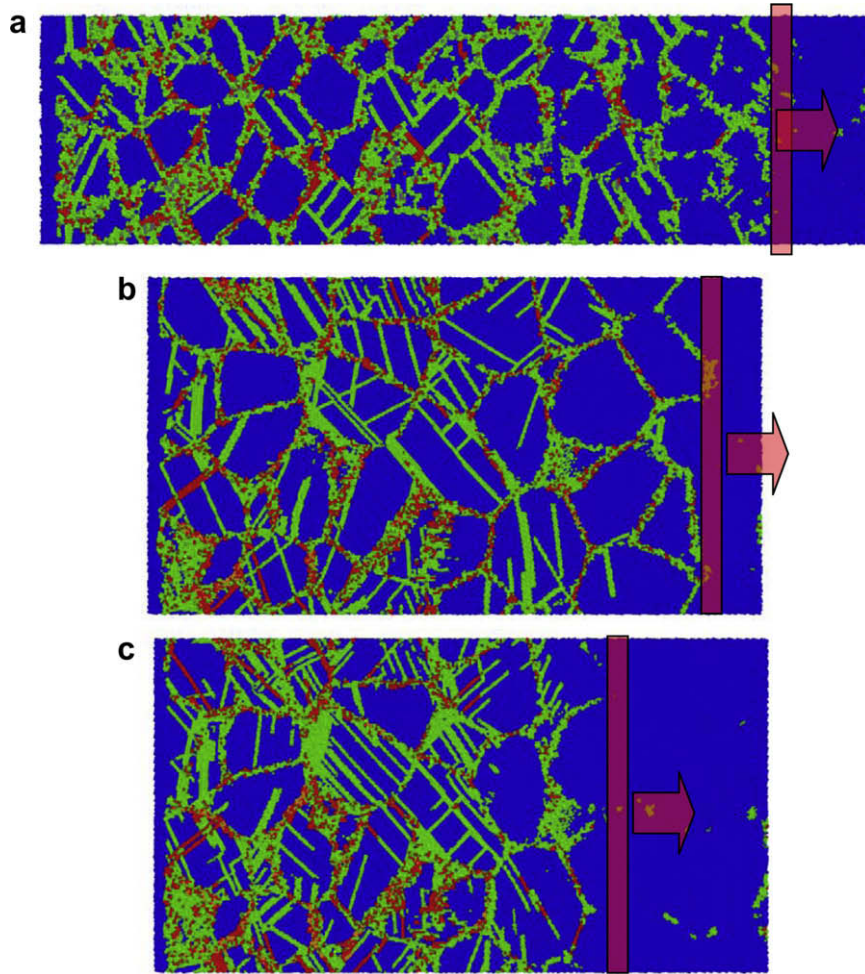


Fig. 11. Comparison of deformation structure for same particle velocity of $U_p = 0.67 \text{ mm}/\mu\text{s}$ (a) 5 nm Ni; (b) 10 nm Ni; (c) 10 nm Cu (position of shock front marked for the three samples).

boundaries highlighted in green. This is due to the fact that no grain-boundary sliding is taking place because the shock front has not yet traveled through that region. The contribution due to partials is comparable in the 5 and 10 nm grain-sized samples, but that from perfect dislocations is greater in the 10 nm samples. Interestingly, the twinning contribution is greater in the 5 nm grain-sized sample (5 nm Ni: 25.7%, 10 nm Ni: 15.7%). This result is in agree-

ment with the models proposed by Chen et al. [58] and Zhu et al. [59], where they show that propensity for twinning increases with decreasing grain-size.

Laser-shock compression experiments were carried out on nc Ni [31,32], with grain sizes between 30 and 50 nm. The samples in the experiments were prepared by electrodeposition at the Lawrence Livermore National Laboratory and were subjected to pressures between 20 and 70 GPa

Table 1

Strain contributions due to various mechanisms in MD specimens shocked at a piston/particle velocity of $U_p = 0.67 \text{ km s}^{-1}$ (total strain of 0.13)

	(1) Twins ($\times 10^{-2}$)	(2) Partials ($\times 10^{-2}$)	(3) Perfect ($\times 10^{-2}$)	(4) >1 dislocation in slip plane ($\times 10^{-2}$)	(5) Correction factor	(6) Total strain due to dislocations ($\times 10^{-2}$)	(7) Grain-boundary shear ($\times 10^{-2}$)
Ni 5 nm (shock)	0.00355	0.0118	0.00142	0.000101	0.00053	0.0138	0.116
Ni 5 nm (shock- release)	0.0029	0.0073	0.00182	0.000533	0.00045	0.01	–
Ni 10 nm (shock)	0.0032	0.0159	0.0035	0.000319	0.00059	0.0203	0.075
Cu 10 nm (shock)	0.0042	0.0164	0.0045	0.000352	0.00058	0.0218	0.075

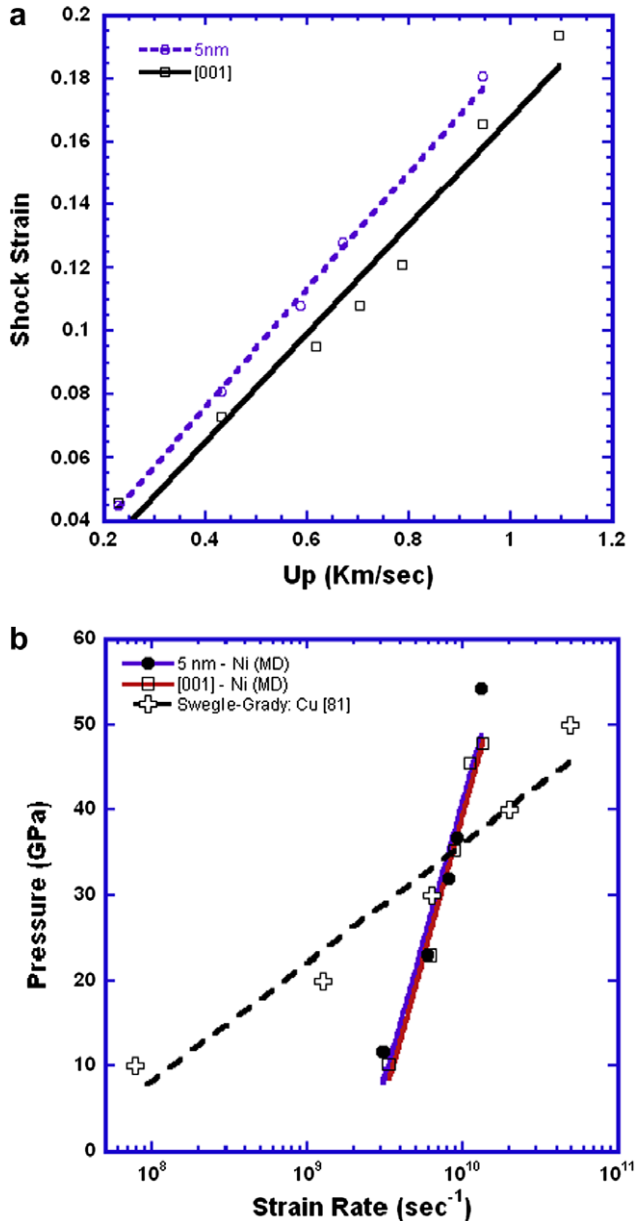


Fig. 12. (a) Shock strain vs. piston velocity; (b) pressure vs. strain rate: comparison between Swegle–Grady relation [72] and MD simulations.

via laser. The microhardness of the samples after shock compression was measured, and a 5–30% increase after shock was observed, clearly indicating dislocation storage. Fig. 13a shows a cross-section of a sample with microhardness measurements taken at five positions beneath the cratered surface. Fig. 13b shows the increase in hardness beneath the cratered surface (a maximum at position 3 occurs where laser intensity (i.e. deformation is greatest), and Fig. 13c shows the increase in hardness due to shock compression of the samples. In congruence with the hardness data, transmission electron microscopy (TEM) examination revealed heavy dislocation activity ($\rho \sim 10^{16} \text{ m}^{-2}$) due to laser shock. Full dislocations were the main carriers of plasticity (Fig. 14a). Interestingly, deformation twins

were not observed in any of the samples, even at pressures up to 70 GPa. This is discussed in Section 6.

To further reduce the grain size to $\sim 10 \text{ nm}$, tungsten (13 wt.%) was added to the Ni electrolyte during electro-deposition as outlined by Schuh et al. [60,61]. The Ni–W samples were loaded to pressures of up to $\sim 38 \text{ GPa}$, and a shift in deformation mechanisms was observed. TEM revealed that deformation twins were the predominant defect structures, indicated by circles in Fig. 14b. A very low density of pre-existing annealing twins was observed in the as-prepared samples, and the twin density of shock loaded samples increased dramatically after shock loading. However, the addition of W lowers the SFE, and the increased twinning cannot be attributed to the decreased grain size alone.

This discrepancy in dislocation behavior between simulations and actual experiments could be due to several factors. The samples in the experiments go through release, which leads to the annihilation and reabsorption of partials. There may be a grain size effect at play. Smaller grains favor partial dislocations, and one may have to go to larger grain sizes for perfect dislocations to be energetically favorable. The MD potentials may not be very accurate in describing the stacking-fault and twinning energy surfaces, and the value of these surfaces under stress could change considerably. Another possibility may be that the time needed for the emission of full dislocation is much longer than the timescales simulated in MD. Loading and unloading in the laser-shock experiments take place within ~ 6 and $\sim 10 \text{ ns}$, whereas the simulations are in the picosecond range, and hence only capture the initial stages of deformation. Warner et al. [62] recently showed that a full dislocation takes much longer than partials and twins to be emitted from a crack tip.

5.2. Effect of unloading on nc Ni

In an analogous manner to the unloading MD simulations carried out on monocrystals (Fig. 7), the effect of unloading on the deformation structure of nc Ni was studied to provide a more realistic comparison with the experiments. The sample shocked at 38 GPa, $U_p = 0.67 \text{ km s}^{-1}$, was allowed to unload, and the dislocation behavior within the grains was analyzed. Fig. 15a shows the average pressure within the sample as a function of time as it is loaded and unloaded. Fig. 15b shows the sample at 0 ps (before shock), at 11 ps (first ps consisted of equilibration) before it is unloaded, and 18 ps after it has been unloaded to zero pressure. The principal features are stacking-faults, which are mostly emitted from grain boundaries during compression. After unloading, $\sim 38\%$ of the partials are reabsorbed. The red circles show regions where partials are reabsorbed and the black circles indicate the partial dislocations that survive after unloading. The reabsorption of partials causes the contribution due to perfect dislocations to increase from 10.3% before unloading

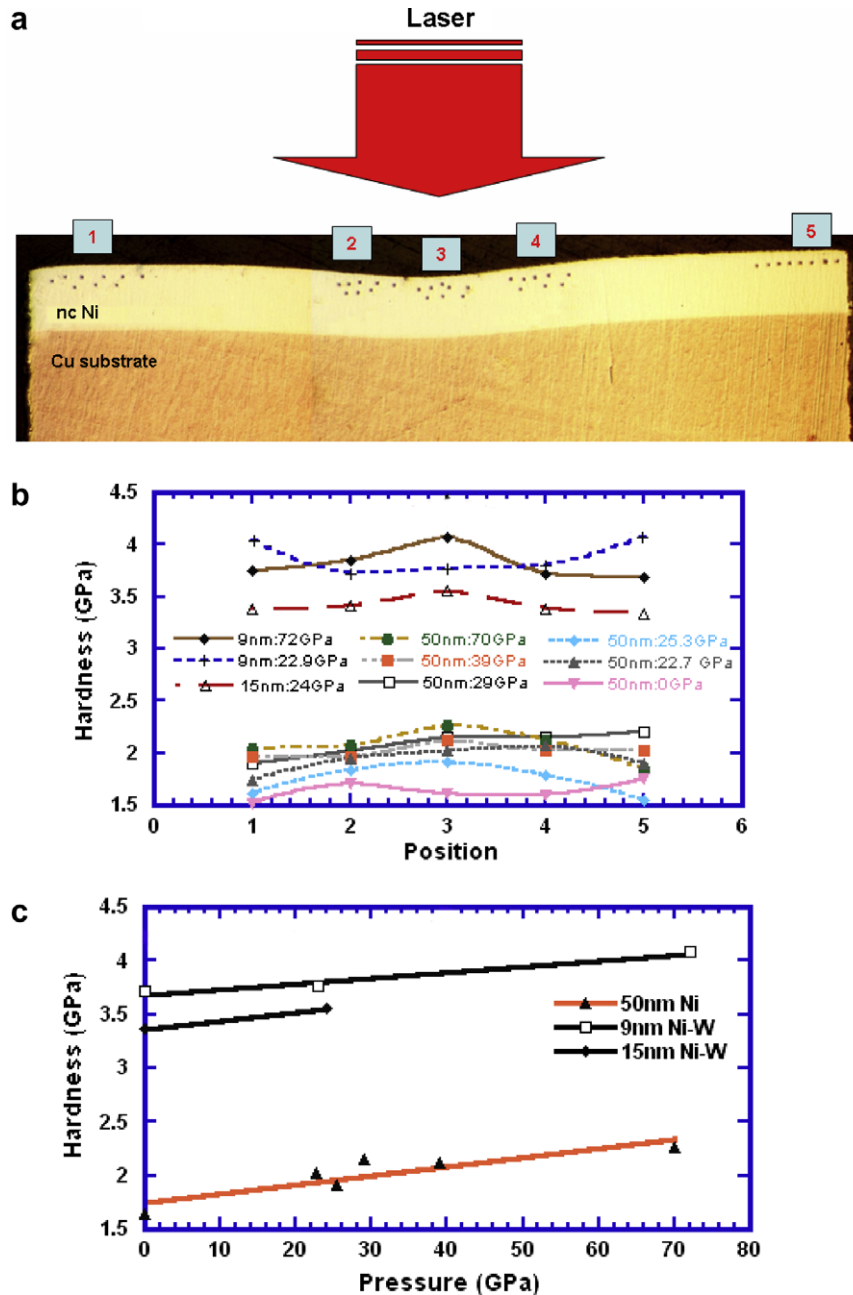


Fig. 13. (a) Cross-sectional microhardness measurements from five positions beneath crater; (b) hardness vs. position; (c) hardness vs. pressure.

to 18.2% after unloading. This phenomenon would explain the fact that partial dislocations are not observed in the experiments, only full dislocations.

For comparison, a smaller sample having $\sim 500,000$ atoms and dimensions of $17.6 \times 17.6 \times 17.6$ nm was compressed uniformly in uniaxial strain to a pressure of ~ 38 GPa and then allowed to unload. The final strain and strain-rate applied were the same as that experienced by the shocked sample, the principal difference being that there is no wave propagation in the latter simulations. Fig. 16a shows the average pressure within the sample as a function of time. The sample was compressed uniaxially for 4 ps to a strain of 0.13, held there for 10 ps, and

released back to 0 strain within 4 ps. Fig. 16b shows the various stages of deformation. Partials are emitted and reabsorbed during this process. Table 2 lists the strain contribution due to the various plastic deformation mechanisms in the sample. There are no major differences in defect distribution between uniform and shock compression. The percentage of strain corresponding to grain-boundary sliding is slightly decreased, as can be seen by comparing Tables 1 and 2. Interestingly, approximately 39% of the partials disappear after unloading. Before unloading, grain-boundary sliding accounts for 79.2% of the total strain, in comparison with shock compression (90%).

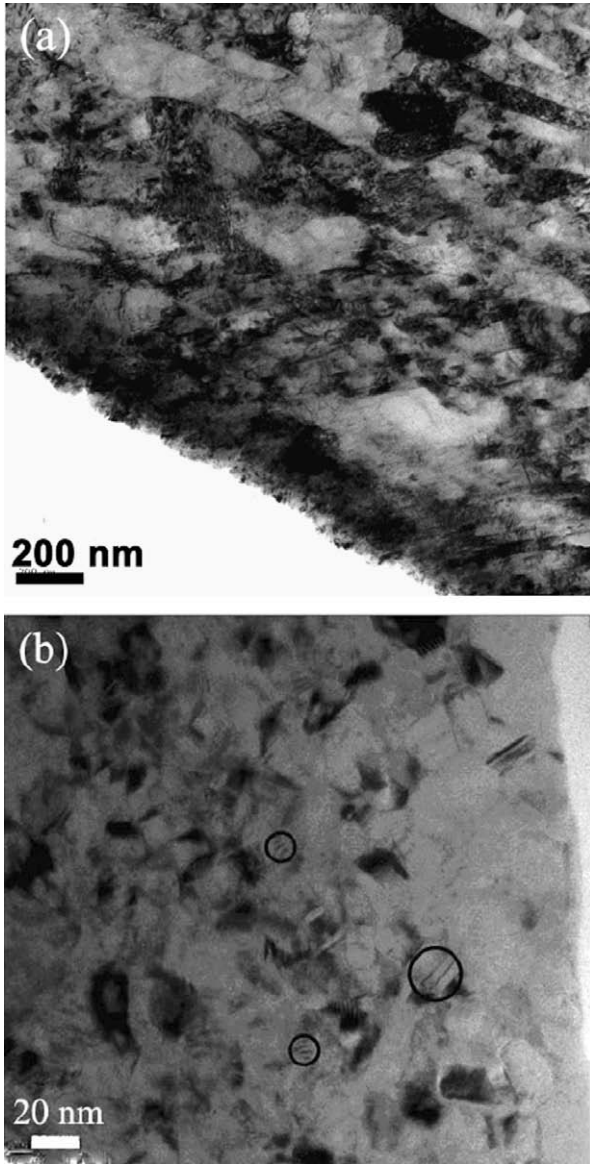


Fig. 14. TEM of Ni with g. s. of 30–50 nm shocked at ~40 GPa showing dislocations; (b) TEM of Ni–W (13 at.%) with g. s. of 10–15 nm shocked at ~40 GPa; deformation twins are evident (circles).

6. The slip-twinning transition in shock compression

The primary aim of this section is to provide a constitutive description of the onset of twinning in Ni and Ni–W subjected to shock compression. The parameters affecting slip and twinning will be discussed first, followed by modeling of the onset of twinning in both materials. Predictions of the model are compared to experimental work carried out on nc Ni and Ni–W at LLNL [31,32].

6.1. Modeling of slip in Ni

The constitutive response for slip of fcc metals is well modeled by the Zerilli–Armstrong (Z–A) constitutive description [63], which captures the essential physical phenomena:

$$\sigma_{\text{slip}} = \sigma_G + C_2 \varepsilon^n \exp(-C_3 T + C_4 T \ln \dot{\varepsilon}) + k_s d^{-1/2}, \quad (15)$$

where σ_G is the athermal component of stress, ε the strain, n the work hardening exponent, d the grain size, T the temperature, k_s the Hall–Petch slope, and C_2 , C_3 and C_4 are constants. For Ni, $\sigma_G = 48.4$ MPa, $C_2 = 2.4$ GPa, $C_3 = 0.0028$ K⁻¹, $C_4 = 0.000115$ K⁻¹ and $k_s = 0.2$ MN m^{-3/2}. The strain-hardening exponent, n , in the nc regime was simply equated to 0 as determined by measurements carried out on the same material by Choi et al. [64]. The values of C_3 and C_4 used are those for Cu [63] since data on Ni was not available. The Ni Hall–Petch slope for slip, k_s , has been established by several researchers [65–67]. Asaro and Suresh [68] compiled hardness data for Ni spanning both the micrometer and nanometer regimes. A k_s value of ~0.2 MN m^{-3/2} was calculated from that set of data. Stress–strain plots of Ni with micrometer-sized grains from Ref. [69] were utilized to establish C_2 . The current model predicts a yield strength of ~1.9 GPa for Ni having a grain size of 30 nm, which is in good agreement with the literature [70,71].

6.2. Modeling of slip in Ni–13 at.% W

Roth et al. [72] obtained the increase in yield stress in Ni as a result of alloying with different elements. They estimate that the flow stress of Ni increases from 100 MPa to approximately 450 MPa due to the addition of 13 at.% W. A plot of the increase in flow stress of Ni with W content is shown in Fig. 17a. The data was extracted from work carried out on Ni having a grain size between 100 and 300 μm . The effect of solid-solution addition to the yield stress increment is as follows:

$$\Delta\sigma_{\text{SS}} = \left(\sum_i K_i^{1/m} C_i \right)^m, \quad (16)$$

where m is ~1/2, K_i is the strengthening constant for solute i , and C_i is the concentration of solute i (for W, $K_i = 977$ MPa at. fraction^{-1/2}). The Z–A equation as a function of W content is obtained by adding the solid-solution term into the athermal component of stress:

$$\sigma_{\text{slip}} = \sigma_G + \left(\sum_i K_i^{1/m} C_i \right)^m + C_2 \varepsilon^n \exp(-C_3 T + C_4 T \ln \dot{\varepsilon}) + k_s d^{-1/2}. \quad (17)$$

The strain-hardening exponent, n , for the nc Ni–W samples was again equated to 0 [64]. The Z–A model predicts a yield strength of ~2.2 GPa for Ni–W with a grain size of 10 nm, very close to the 2.38 GPa value reported by Choi et al. [64]. The Hall–Petch slope, k_s , for Ni–W was estimated using yield strength data on Ni–W samples having grain sizes in the micrometer regime and microhardness measurements carried out on the nc Ni–W samples. A k_s value of 0.1 MPa m^{-3/2} was estimated.

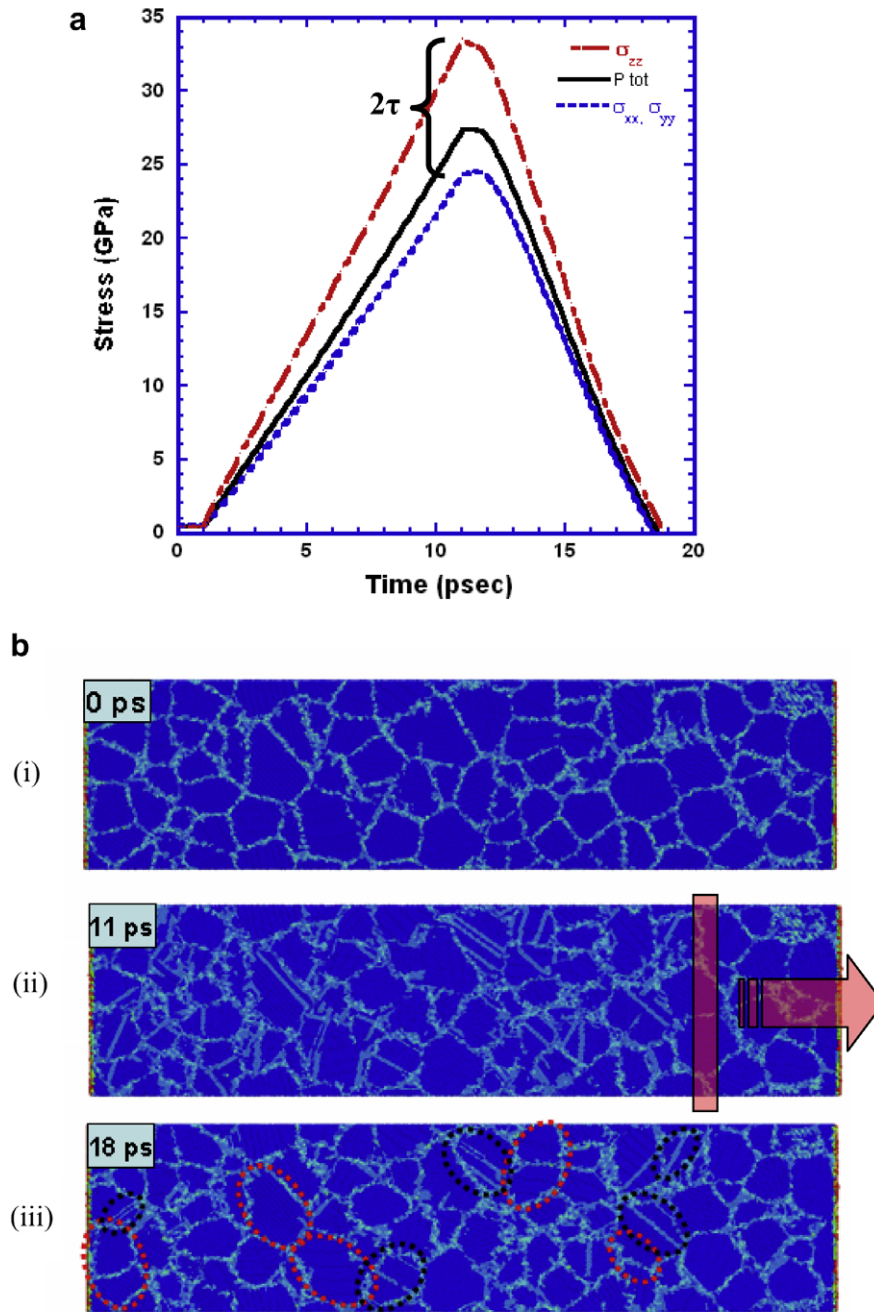


Fig. 15. (a) Average pressure rise and release in sample for $U_p = 0.67$ km/s; (b) deformation features (i) before compression, (ii) at maximum compression, and (iii) release back to zero pressure.

6.3. Modeling of twinning

Despite the fact that dislocation activity is directly associated with twinning, slip by dislocation motion is much more sensitive to strain rate and temperature [73–76], whereas twinning is much less sensitive to these parameters [77]. Fig. 17b shows the twinning shear stresses as a function of temperature for a number of metals. It clearly indicates that the twinning stress is temperature insensitive over the range considered. This trend is actually still subject to debate as results have been conflicting. In their review article on mechanical twinning,

Christian and Mahajan [78] proposed that body-centered cubic (bcc) metals have a negative dependence of twinning stress on temperature, whereas fcc metals have a weakly positive dependence. In the analysis on the onset of twinning that follows, it is assumed that the twinning shear stress is insensitive to temperature, pressure and strain rate.

6.4. Grain-size and stacking-fault energy effects on twinning

The effect of grain size on the twinning stress has been found to be greater than that on the slip stress for many

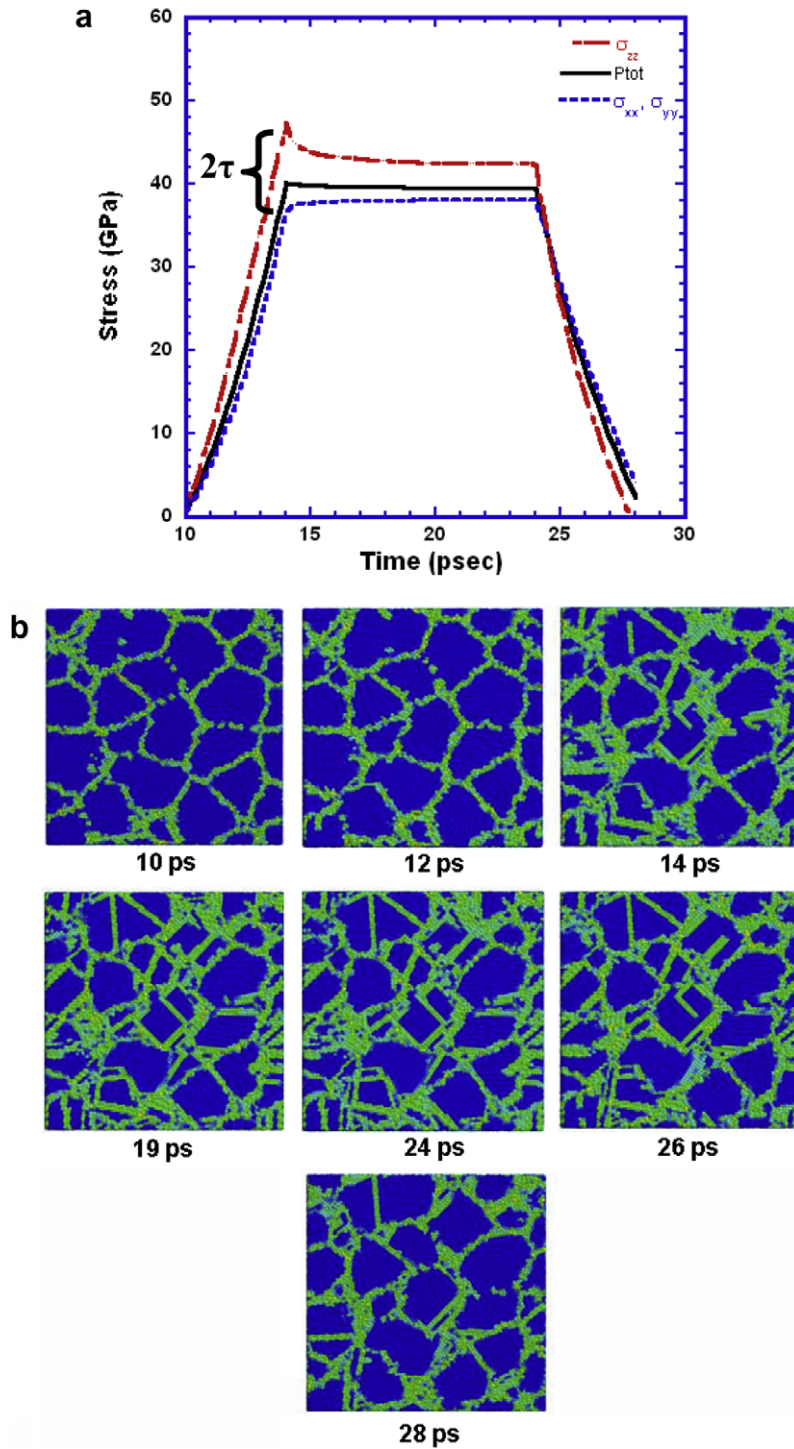


Fig. 16. (a) Uniaxial compression and relaxation of 5 nm grain-sized Ni sample; (b) frames at different times showing emission and annihilation by reabsorption of partial dislocations into grain boundaries.

metals and alloys [79]. A Hall–Petch relationship can, thus, be ascribed to the twinning stress:

$$\sigma_T = \sigma_{T_0} + k_T d^{-1/2}, \tag{18}$$

where k_T is the twinning Hall–Petch slope (higher than the k_s slope for slip), σ_{T_0} is the initial twinning stress assumed for a monocrystal ($\lim_{d \rightarrow \infty} (d^{-1/2}) = 0$), and d is grain size. Haasen

[80] carried out low-temperature tensile tests on monocrystalline Ni and observed twinning at 4.2 and 20 K at a shear stress considerably higher than that for Cu. This shear stress was estimated to be equal to 250–280 MPa, which is equivalent to a normal stress, σ_{T_0} , of 500–560 MPa.

Meyers et al. [81] conducted shock compression experiments on Cu up to pressures of 35 GPa. They detected an

Table 2

Strain contribution due to various mechanisms in MD specimen uniformly and uniaxially compressed to a total strain of 0.13

	(1) Twins ($\times 10^{-2}$)	(2) Partials ($\times 10^{-2}$)	(3) Perfect ($\times 10^{-2}$)	(4) >1 dislocation in slip plane ($\times 10^{-2}$)	(5) Correction factor	(6) Total strain due to dislocation ($\times 10^{-2}$)	(7) Grain-boundary shear ($\times 10^{-2}$)
Ni 5 nm (uniaxial compression)	0.0067	0.0212	0.00374	0.0003608	0.00144	0.0267	0.103
Ni 5 nm (uniaxial release)	0.0049	0.0129	0.00334	0.001026	0.00074	0.0181	–

abundance of twins for grain sizes between 100 and 300 μm , but found no traces of twinning at a grain size of $\sim 10 \mu\text{m}$. Similar results were obtained by Sanchez et al. [82]. Vöhringer [83] established that the twinning Hall–Petch slope for Cu, k_T , is $\sim 0.7 \text{ MN m}^{-3/2}$, which is significantly higher than that for slip, $k_s \sim 0.3 \text{ MN m}^{-3/2}$. In the present modeling of Ni, it is assumed that k_T for Ni is three times k_s . Thus, a k_T value of $0.6 \text{ MN m}^{-3/2}$ is used for Ni.

Solid-solution strengthening and SFE effects are incorporated into the slip-twinning model as a result of alloying with W. The addition of solute atoms hinders the move-

ment of dislocations, hence creating a strengthening effect [84]. Alloying also significantly reduces the SFE, γ_{sf} . For instance, it has been shown that the SFE of Cu decreases by nearly 50% by the addition of 2 wt.% Al [35]. This effect is related to the change in the electron to atom ratio (e/a). Partial dislocations are under elastic equilibrium, where the repulsive forces between the bounding partials are balanced by the forces needed to minimize the stacking-fault area and maintain a minimum energy configuration. Thermodynamically, alloying can alter the difference in the free energy between the hexagonal close packed (hcp, stacking-fault ribbon) and fcc structures and, therefore, the

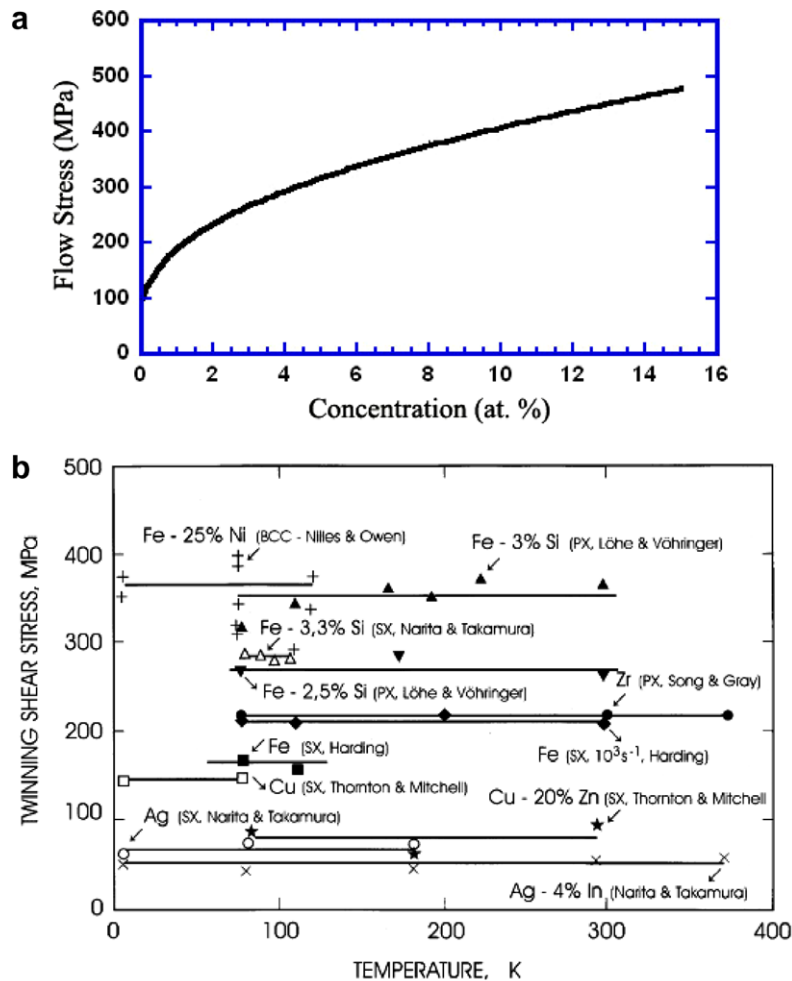


Fig. 17. (a) Slip stress of Ni as a function of the concentration of W (at.%); (b) twinning stress as a function of temperature for a number of metals – both mono and polycrystals (from Meyers et al. [78]).

energy of the ribbon between two partials as well as their separation.

It is well-established in the literature that the twinning stress, τ_T , varies with SFE. Venables [85,86] and Vöhringer [87,88] performed extensive analyses on the twinning stress for a number of alloys and found that it varies with the square root of the SFE:

$$\tau_T = k \left(\frac{\gamma_{sf}}{Gb_S} \right)^{1/2}, \quad (19)$$

where, k is a proportionality constant and G is the shear modulus. Eq. (4) has been incorporated into our analysis. A k value of 6.8 GPa was estimated for Ni alloys. The shear modulus and SFE of Ni as a function of W concentration can be found in work by Tearney et al. [89]. At 13 at.% W content (that present in the nc Ni–W samples), a shear modulus of 88 GPa and SFE of 52.5 mJ m⁻² (60% drop in SFE) are reported.

Assuming a twinning Hall–Petch slope three times that of slip, a k_T value for Ni–W equal to 0.3 MPa m^{-3/2} is obtained. Just as in the case of pure Ni, a Hall–Petch behavior accounting for the effect of grain size on the twinning stress is adopted in predicting the critical twinning transition pressure in Ni–W (13 at.%). The following expression for the twinning stress was used:

$$\sigma_T = k \left(\frac{\gamma_{sf}}{Gb_S} \right)^{1/2} + k_{T_{NiW}} d^{-1/2}. \quad (20)$$

For Ni–13 at.% W, $k = 6.8$ GPa, $k_{T_{NiW}} = 0.3$ MPa, $\gamma_{sf} = 52.5$ mJ m⁻², $G = 88$ GPa, $b_S = 0.249$ nm.

6.5. Critical pressure for slip-twinning transition

In this analysis, it is assumed that the transition from slip to twinning occurs when the shear stress for twinning, τ_T , becomes equal to or less than the shear stress for slip, τ_S :

$$\tau_T \leq \tau_S. \quad (21)$$

If one uses the same conversion parameters:

$$\sigma_T \leq \sigma_S. \quad (22)$$

This is a reasonable approximation since both mechanisms are subjected to the same stress system at the shock front. It should be mentioned that the criterion described here is based on the critical shear stresses for slip and twinning; the pressure only enters insofar as it determines the shear stress and strain rate.

We assume the twinning stress, σ_T , to be pressure and temperature independent. The dependence of shock pressure on strain rate for Ni, obtained through the Swegle–Grady relationship [90], is not available in the literature. As an approximation, the strain rate vs. pressure behavior of Cu is adopted. The reasoning for this approximation is that Al and Cu, both fcc metals, have a strain-rate response to shock pressure that is very comparable even though the stacking-fault energy of

Al is much higher. One would expect that the behavior of Ni should not significantly deviate from that of Al and Cu. Thus, the Swegle–Grady relationship for Ni is given as follows:

$$\dot{\epsilon} = 7.84 \times 10^{-33} \times P_{shock}^4. \quad (23)$$

Two separate aspects have to be considered in the analysis: (i) plastic strain at the shock front, and (i) shock heating. Both plastic strain by slip (and associated work hardening) and shock heating alter the flow stress of a material by slip processes and need to be incorporated into the computation. The total (elastic + plastic) uniaxial strain, ϵ , at the shock front is related to the change in specific volume by [39]:

$$\frac{V}{V_0} = e^\epsilon. \quad (24)$$

The pressure dependence on strain, determined from the Rankine–Hugoniot equations, equation of state, and Eq. (24) is expressed as follows [39]:

$$P_{shock} = \frac{C_0^2(1 - e^\epsilon)}{V_0[1 - S(1 - e^\epsilon)]^2}. \quad (25)$$

The associated temperature rise in Ni as a function of shock pressure is represented by Eq. (26), which is a polynomial that was generated from thermodynamically calculated data in Ref. [39]:

$$T_{shock} = 8 \times 10^{-20} \times P_{shock}^2 + 9 \times 10^{-10} \times P_{shock} + 301.5 \text{ K}. \quad (26)$$

For Ni–W, the temperature rise and strain associated with a given shock pressure are determined just as outlined in the case for pure Ni.

Fig. 18a shows both the slip stress, σ_S (incorporating thermal softening, strain-rate hardening and work hardening) and σ_T as a function of pressure for Ni. The point at which the horizontal line determined by σ_T , Eq. (22), intersects the slip stress at a given shock pressure, is defined as the critical twinning transition pressure. This transition pressure for Ni with a grain size of 30 nm was found to be ~78 GPa and is consistent with the fact that twins are not observed in experiments up to pressures of ~70 GPa. The result of the twinning transition pressure for nc Ni–13 at.% W, having a grain size of 10 nm, is illustrated in the plot in Fig. 18b. It is equal to 16 GPa, and is consistent with experiments where twins were observed at pressures of ~38 GPa.

The slip-twinning transition pressure as a function of grain size (micro- to nanometer regime) was also calculated. The strain-hardening exponent was varied between $n = 0.5$ in the micrometer regime (as determined by fitting to stress–strain plots found in Andrade [69]) and $n = 0$ in the nanometer regime [64]. The result is shown in Fig. 19. It clearly shows the much higher transition pressure in Ni as compared to Ni–W as well as the effect of grain size on the slip-twinning transition.

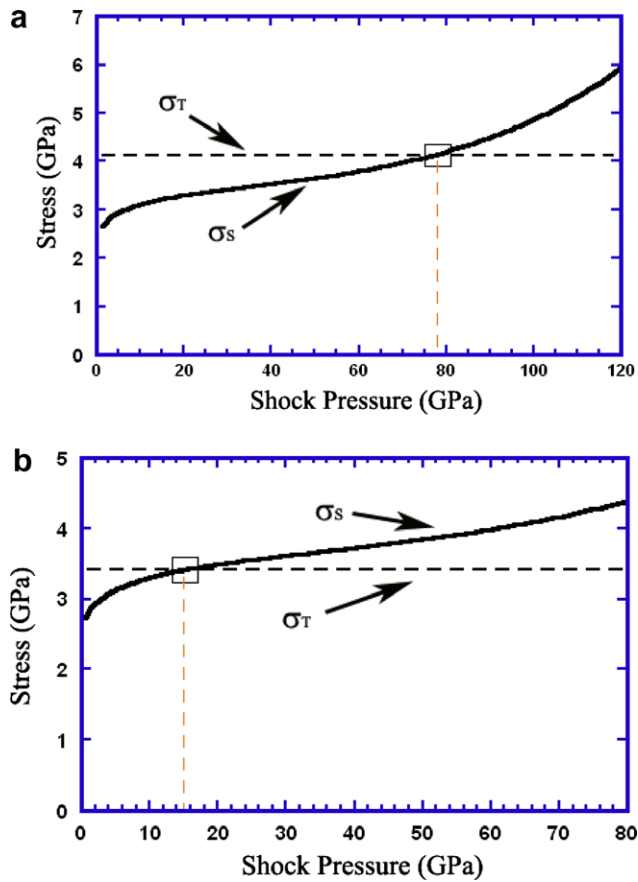


Fig. 18. (a) Slip and twinning stress vs. shock pressure for nanocrystalline nickel (g. s. = 30 nm); twinning threshold ~ 78 GPa.; (b) slip and twinning stress vs. shock pressure for Ni-W (13 at.%) having a grain size of 10 nm; twinning transition takes place at ~ 16 GPa.

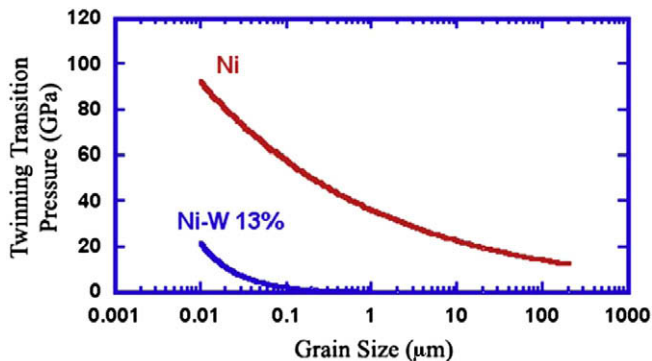


Fig. 19. Calculated twinning transition pressure vs. grain size for Ni and Ni-13 at.% W.

7. Conclusions

7.1. Monocrystalline Ni

- Molecular dynamics simulations of shock compression of [001] Ni provided a constitutive response consistent with Hugoniot data from experiments by Rice et al.

[38]. Partial dislocation loops were emitted at the shock front along the {111} slip systems, consistent with the early homogeneous dislocation generation model [14].

- The pressure at which a transition from dislocation cells to stacking-faults occurs in Ni was found to be 27 GPa, close to the experimentally observed twinning pressure of 35 GPa.
- The analytical calculations of the cell-stacking fault and slip-twinning transitions in monocrystalline Ni are:
 - Cells \rightarrow stacking-faults: $P \sim 27$ GPa
 - Slip \rightarrow twinning: $P \sim 15$ GPa

In contrast, for monocrystalline Cu, they are [49]:

- Cells \rightarrow stacking-faults: $P \sim 5$ GPa
- Slip \rightarrow twinning: $P \sim 50$ GPa

The experimental results corroborate the analysis, which shows that Ni twins at a pressure below the stacking-fault formation; thus, individual stacking-faults are not observed [44]. On the other hand, for Cu, the stacking-fault transition occurs at a lower pressure than the twin threshold, and a stacking-fault regime is predicted and is indeed observed at intermediate pressures [52,53].

7.2. Nanocrystalline Ni

- The MD simulations predict dislocation densities orders of magnitude larger than the ones observed experimentally, confirming earlier comparisons in Cu by Cao et al. [12]. The cause for this discrepancy is identified: upon unloading from the peak pressure, the majority of dislocations generated in shock compression is annihilated. This suggests that previous observations of residual structures bear little resemblance to the defect configuration during compression.
- The various contributions to the shock strain were estimated, and it was found that grain-boundary sliding accounts for 58–90% of the total.
- The total strain due to dislocations was analyzed in the nc Ni samples, and it was mainly governed by partial dislocations, where grains acted as sources and sinks. The effects of grain-size (5 nm vs. 10 nm) and a different potential (Ni vs. Cu) were studied. Slightly more twinning was observed in Cu, as expected. Grain-boundary sliding was found to be slightly less in the 10 nm grain-size sample since it is more difficult for larger grains to shear past each other. More twinning was also favored for the smaller 5 nm Ni sample as compared to the 10 nm Ni sample.
- An analytical model of the slip-twinning transition in nc Ni (grain size ~ 30 nm) under shock compression predicts a critical twinning pressure of 78 GPa, consistent with TEM observations at the same grain size which show no evidence of twinning at shock pressures up to 70 GPa.

- The same model applied to nc Ni–W (grain size ~ 10 nm) under shock compression predicts a critical twinning pressure of 16 GPa, consistent with TEM observations that show twin formation in nc Ni–W (grain size 10–15 nm) at a shock pressure of 38 GPa.

Acknowledgments

This work was funded by the UCOP through the Institute for Laser Science and Applications, under ILSA Contract No. W-7405-Eng-48. The Ni–W specimens were kindly provided by Prof. C. Schuh, MIT. The help provided by Dr. D. Correll is gratefully acknowledged. Parts of this work were also supported by US DOE-BES, under Grant No. DEFG02-91ER45439.

References

- [1] Holian BL, Straub GK. *Phys Rev Lett* 1979;43:1598.
- [2] Holian BL, Hoover WG, Moran B, Straub GK. *Phys Rev A* 1980;22:2498.
- [3] Holian BL. *Phys Rev A* 1988;37:2562.
- [4] Holian BL, Lomdahl PS. *Science* 1998;280:2085.
- [5] Germann TC, Holian BL, Lomdahl PS. *Phys Rev Lett* 2000;84:5351.
- [6] Tanguy D, Mareschal M, Lomdahl PS, Germann TC, Holian BL, Ravelo R. *Phys Rev B* 2003;68:14111.
- [7] Germann TC, Holian BL, Lomdahl PS, Tanguy D, Mareschal M, Ravelo R. *Metall Mater Trans A* 2004;35A:2609.
- [8] Taylor PA, Dodson BW. *Phys Rev B* 1990;42:1200.
- [9] Holian BL, Voter AF, Wagner NJ, Ravelo RJ, Chen SP, Hoover WG, et al. *Phys Rev A* 1991;43:2655.
- [10] Ryazanov AI, Dremov VV, Kiritani M. *Radiat Eff Defects Solids* 2002;157:209.
- [11] Bringa EM, Cazamias JU, Erhart P, Stolken J, Tanushev N, Wirth BD, et al. *J Appl Phys* 2004;96:3793.
- [12] Cao B, Bringa EM, Meyers MA. *Metall Mater Trans A* 2007;38:1073.
- [13] Smith CS. *Response of metals to high velocity deformation*. New York: Interscience; 1961. p. 483–486.
- [14] Meyers MA. *Scripta Metall* 1978;12:21.
- [15] Foreman AJE, English CA, Phythian W. *J Philos Mag* 1992;A66:655.
- [16] Mishin Y, Mehl MJ, Papaconstantopoulos DA, Voter AF, Kress JD. *Phys Rev B* 2001;63:224106.
- [17] Kum OJ. *Appl Phys* 2003;93:3239.
- [18] Van Swygenhoven H, Caro A. *Phys Rev B* 1998;58:11246.
- [19] Schiøtz J, Di Tolla FD, Jacobsen KW. *Nature* 1998;391:561.
- [20] Van Swygenhoven H, Spaczer M, Caro A, Farkas D. *Phys Rev B* 1999;60:22.
- [21] Yamakov V, Wolf D, Phillpot SR, Mukherjee AK, Gleiter H. *Nat Mater* 2002;1:45.
- [22] Schiøtz J, Jacobsen KW. *Science* 2003;31:1357.
- [23] Van Swygenhoven H, Derlet PM, Frøseth AG. *Nat Mater* 2004;3:399.
- [24] Finnis M, Sinclair M. *Philos Mag A* 1984;50:45.
- [25] Jacobsen KW, Nørskov JK, Puska MJ. *Phys Rev B* 1987;35:7423.
- [26] Jacobsen KW, Stoltze P, Nørskov JK. *Surf Sci* 1996;366:394.
- [27] Ercolessi F, Adams JB. *Europhys Lett* 1994;26:583.
- [28] Bringa EM, Caro A, Wang Y, Victoria M, McNaney JM, Remington BA, et al. *Science* 2005;309:1838.
- [29] Dremov V, Petrovtsev A, Sapozhnikov P, Smirnova M. *Phys Rev B* 2006;74:144110.
- [30] Sapozhnikov FA, Dremov VV, Smirnova MS. *J Phys IV France* 2003;110:323.
- [31] Wang YM, Bringa EM, McNaney JM, Victoria M, Caro A, Hodge AM, et al. *Appl Phys Lett* 2006;88:061917.
- [32] Wang YM, Bringa EM, Victoria M, Caro A, McNaney JM, Smith R, et al. *J Phys IV France* 2006;134:915–20.
- [33] Plimpton SJ. *J Comput Phys* 1995;117:1–19. Available from: <http://lammmps.sandia.gov>.
- [34] Mishin Y, Farkas D, Mehl MJ, Papaconstantopoulos DA. *Phys Rev B* 1999;59:3393.
- [35] Murr LE. *Interfacial phenomena in metals and alloys*. Reading, MA: Addison-Wesley; 1975.
- [36] Daw MS, Baskes MI. *Phys Rev Lett* 1983;50:1285.
- [37] Daw MS, Baskes MI. *Phys Rev B* 1984;29:6443.
- [38] Rice MH, McQueen RG, Walsh JM. *Solid State Phys* 1958;6:1.
- [39] Meyers MA. *Dynamic behavior of materials*. New York: John Wiley; 1994.
- [40] Nolder RL, Thomas G. *Acta Metall* 1963;11:994.
- [41] Greulich F, Murr LE. *Mater Sci Eng* 1979;39:81.
- [42] Esquivel EV, Murr LE, Trillo EA, Baquera MJ. *Mater Sci* 2003;38:2223.
- [43] Kelchner CL, Plimpton S, Hamilton JC. *Phys Rev B* 1998;58:11085.
- [44] Murr LE. In: *Shock waves and high-strain rate phenomena in metals*. New York: Plenum Press; 1981. p. 607–73.
- [45] Cottrell A. *Dislocations and plastic flow in crystals*. Oxford: Clarendon Press; 1953. p. 54.
- [46] Xu G, Argon AS. *Philos Mag* 2000;80:605.
- [47] Rice JR. *J Mech Phys Solids* 1992;40:256.
- [48] Khantha M, Vitek V. *Acta Mater* 1997;45:4675.
- [49] Meyers MA, Schneider MS, Jarmakani H, Kad B, Remington BA, Kalantar DH, et al. *Metall Mater Trans* 2008;39A:304.
- [50] Hull D, Bacon DJ. *Introduction to dislocations*. Oxford: Butterworth-Heinemann; 2001. p. 147.
- [51] Preston DL, Wallace DC. *Solid State Commun* 1992;81:277.
- [52] Schneider MS, Kad BK, Kalantar DH, Remington BA, Meyers MA. *Metall Mater Trans A* 2004;35A:2633.
- [53] Schneider MS, Kad BK, Kalantar DH, Remington BA, Kenik E, Jarmakani H, et al. *Int J Impact Eng* 2005;32:473.
- [54] Meyers MA, Jarmakani H, McNaney JM, Schneider M, Nguyen JH, Kad B. *J Phys IV France*. 2006:13437.
- [55] Kadav K, Germann TC, Lomdahl PS, Holian BL, Kadav D, Ental P, et al. *Metall Mater Trans A* 2004;35A:2719.
- [56] Odunuga S, Li Y, Krasnochtchikov P, Bellon P, Averback RS. *Phys Rev Lett* 2005;95:045901.
- [57] Vo NQ, Odunuga S, Bellon P, Averback RS, Caro A. *Phys Rev B* 2008;77:1341086.
- [58] Chen M, Ma E, Hemker KJ, Sheng H, Wang Y, Cheng X. *Science* 2003;300:1275.
- [59] Zhu YT, Liao XZ, Srinivasan SG, Zhao YG, Baskes MI. *Appl Phys Lett* 2004;85:5049.
- [60] Schuh CA, Nieh TG, Yamasaki T. *Scripta Mater* 2002;46:735.
- [61] Schuh CA, Nieh TG, Iwasaki H. *Acta Mater* 2003;51:431.
- [62] Warner DH, Curtin WA, Qu S. *Nat Mater* 2007;6:876.
- [63] Zerilli FJ, Armstrong RW. *J Appl Phys* 1987;61:1816.
- [64] Choi IS, Detor AJ, Schwaiger R, Dao M, Schuh CA, Suresh S. *J Mech Phys Solids* 2008;56:172.
- [65] Thompson AW. *Acta Metall* 1975;23:1337.
- [66] Thompson AW. *Acta Metall* 1977;25:83.
- [67] Thompson AW, Baskes MI, Flanagan WF. *Acta Metall* 1973;21:1017.
- [68] Asaro R, Suresh S. *Acta Mater* 2005;53:3369.
- [69] Andrade U. *Doctoral thesis*. UCSD; 1993.
- [70] Dalla Torre F, Van Swygenhoven H, Victoria M. *Acta Mater* 2002;50:3957.
- [71] Schwaiger R, Moser B, Dao M, Chollacoop N, Suresh S. *Acta Mater* 2003;51:5159.
- [72] Roth HA, Davis RC, Thomson RC. *Metall Trans A* 1997;28A:1329.
- [73] Becker RZ. *Phys* 1925;26:919.
- [74] Seeger AZ. *Naturforsch* 1954;26:758.
- [75] Seeger AZ. *Naturforsch* 1954;26:818.
- [76] Seeger AZ. *Naturforsch* 1954;26:851.

- [77] Meyers MA, Vöhringer O, Lubarda VA. *Acta Mater* 2001;49:4025.
- [78] Christian JW, Mahajan S. *Prog Mater Sci* 1995;39.
- [79] Armstrong RW, Worthington PJ. In: Rohde RW, Butcher BM, Holland JR, Karnes CH, editors. *Metallurgical effects at high strain rates*. New York: Plenum Press; 1973. p. 401–14.
- [80] Haasen P. *Philos Mag* 1958;3:384.
- [81] Meyers MA, Andrade UR, Chokshi AH. *Metall Mater Trans* 1995;26A:2881.
- [82] Sanchez JC, Murr LE, Staudhammer KP. *Acta Mater* 1997;45:3223.
- [83] Vöhringer OZ. *Z Metallk* 1976;67:51.
- [84] Honeycombe RWK. *The plastic deformation of metals*. London: Edward Arnold; 1984.
- [85] Venables JA. *Philos Mag* 1961;6:379.
- [86] Venables JA. In: Reed-Hill RE, Hirth JP, Rogers HC, editors. *Deformation twinning*. New York: Gordon and Breach; 1964.
- [87] Vöhringer OZ. *Z Metallk* 1974;65:352.
- [88] Vöhringer OZ. *Z Metallk* 1972;11:1119.
- [89] Tearney TC, Grant NJ. *Metall Trans A* 1982;13A:1827.
- [90] Swegle JW, Grady DE. In: Gupta YM, editor. *Shock waves in condensed matter* 1985. New York: Plenum Press; 1986.